Cargo Pendulation Reduction on Ship-Mounted Cranes

Ryan J. Henry

Thesis submitted to the Faculty of the
Virginia Polytechnic Institute and State University
in partial fulfillment of the requirements for the degree of

Master of Science
in
Engineering Mechanics

Ali H. Nayfeh, Chair
Scott L. Hendricks
Dean T. Mook

June 24, 1999
Blacksburg, Virginia

Keywords: Crane control, ship-mounted crane, time-delayed feedback

Cargo Pendulation Reduction on Ship-Mounted Cranes

Ryan J. Henry

(ABSTRACT)

It is sometimes necessary to transfer cargo from a large ship to a smaller ship at sea. Specially designed craneships are used for this task, however the wave-induced motions of the ship can cause large pendulations of cargo being hoisted by a ship-mounted crane. This makes cargo transfer in rough seas extremely dangerous and therefore transfer operations normally cease when sea state 3 is reached. If the cargo pendulations could be reduced in higher sea states, transfer operations would be possible.

By controlling the boom luff angle, one can reduce the cargo pendulations in the plane of the boom significantly. A two-dimensional pendulum with a rigid massless cable and massive point load is used to model the system. A control law using time-delayed position feedback is developed and the system is simulated on a computer using the full nonlinear equations of motion. A three-degree-of-freedom ship-motion simulation platform, capable of simulating heave, pitch, and roll motions, was built. The computer simulation results were experimentally verified by mounting a 1/24th scale model of a T-ACS crane on the ship-motion simulation platform.

This work was supported by the Office of Naval Research under Contract #N00014-96-1-1123.

To my Mother and Father

Acknowledgments

There are many people without whom this thesis would not have been possible. First I would like to thank Dr. Ali Nayfeh and Dr. Dean Mook for their guidance, support, and trust throughout the past two years. It was a true pleasure to work with two so highly distinguished professors. I would also like to thank my other committee member, Dr. Scott Hendricks, for his instruction over the years. His dedication, knowledge, and humor made him one of the best teachers I have ever had. There are many other faculty members, too numerous to list, to whom I am grateful.

Sally Shrader deserves a special thanks for all of her hard work. She was always willing to go out of her way to lend a helping hand. I am indebted to my fellow students in the Nonlinear Dynamics and Vibration Research Group, especially Ziyad Masoud and Ben Hall, for their assistance. Ziyad worked diligently with me for most of the last two years. In addition to developing creative solutions to all sorts of problems that we encountered, he kindly performed the never ending task of pointing out all of my mistakes. Ben helped me with classwork, taught me countless tricks in different software packages, suggested solutions to numerous research problems, and kept me laughing through it all.

I am especially grateful to my parents. All of my accomplishments are a product of their support and love. Finally, I would like to thank all of my friends who made the last two years a lot of fun and kept me sane during stressful times.

Contents

List of Figures

List of Tables

Chapter 1

Introduction

1.1 Cargo Transfer at Sea

It is sometimes necessary to unload large cargo ships at sea and transfer their cargo to shore without the aid of fixed port facilities. The ships unloaded during these operations include containerships, roll-on/roll-off ships, heavy lift barge carriers, semi-submersible ships, and deep draft tankers. The military has developed many subsystems capable of transferring cargo, such as containers, military equipment, and fuel from these ships to the shore. These activities known to the military as Logistics Over the Shore (LOTS) operations. Often these operations are carried out with the aid of more than one branch of military service, in which case they are called Joint Logistics Over the Shore (JLOTS) operations. [22]

Military requirements state that LOTS operations should be capable of being performed in sea state 0 through sea state 3 conditions (see Table 1.1). In order to evaluate operational capabilities, several JLOTS exercises have been conducted in the past. JLOTS I was conducted in 1976-1977 and demonstrated limitations in cargo throughput during rough sea conditions. JLOTS II, conducted in 1983-1984, incorporated some new technology into the exercises;

Table 1.1: Significant wave heights and average periods for several sea states according to the Pierson-Moskowitz sea spectrum [6].

Sea State	Significant Wave Height, ft	Average Period, sec
0	< 0.5	0.5 - 1.0
1	0.5 - 1.0	1.5 - 2.0
2	1.5 - 3.0	2.5 - 3.5
3	3.5 - 5.0	3.5 - 4.5
4	6.0 - 7.5	5.0 - 5.5
5	8.0 - 12.0	5.5 - 7.0

however, operations were not possible above sea state 2. Recently, several new subsystems were tested during JLOTS III in 1991-1993, but operations again ceased when sea state 3 was reached. Sea state 3 occurs approximately 20% of the time on average around the world and conditions above sea state 3 occur approximately 15% of the time [22]. Therefore, cargo throughput could be increased significantly if operations were possible in sea state 3.

One of the new subsystems evaluated during the JLOTS II exercises was the Auxiliary Crane Ship (T-ACS), shown in Figure 1.1 [22]. The T-ACS are converted container ships with two or three twin boom pedestal cranes that can lift cargo from themselves or adjacent ships and deposit the cargo on a pier or lighterage. Lighterage is a small craft capable of transporting a small amount of cargo or personnel from a ship anchored at sea to the unimproved shore. These vessels include amphibious craft, landing craft, discharge lighters, causeways, and barges [15]. An example of a landing craft vessel is shown in Figure 1.2. Ten T-ACS ships have been built with the first completed in 1984 and the last completed in 1997. The twin boom cranes have a load capacity of 30 LT in single mode and 60 LT in tandem mode. In a typical cargo transfer scenario, shown in Figure 1.3, the T-ACS is positioned between a containership on her starboard-side and lighterage on her port-side. Cargo is transferred from the containership to the lighterage using the T-ACS cranes.

During JLOTS III, operations were halted in sea state 3 due to many problems, including the crews' lack of seamanship skills, the inability of lighterage to moor to ships at anchor, and T-ACS crane load pendulations [22]. As seas became rough the wave-induced ship motions

Figure 1.1: Auxiliary Crane Ship (T-ACS) [8].

Figure 1.2: LCU 2000 vessel unloading cargo [5].

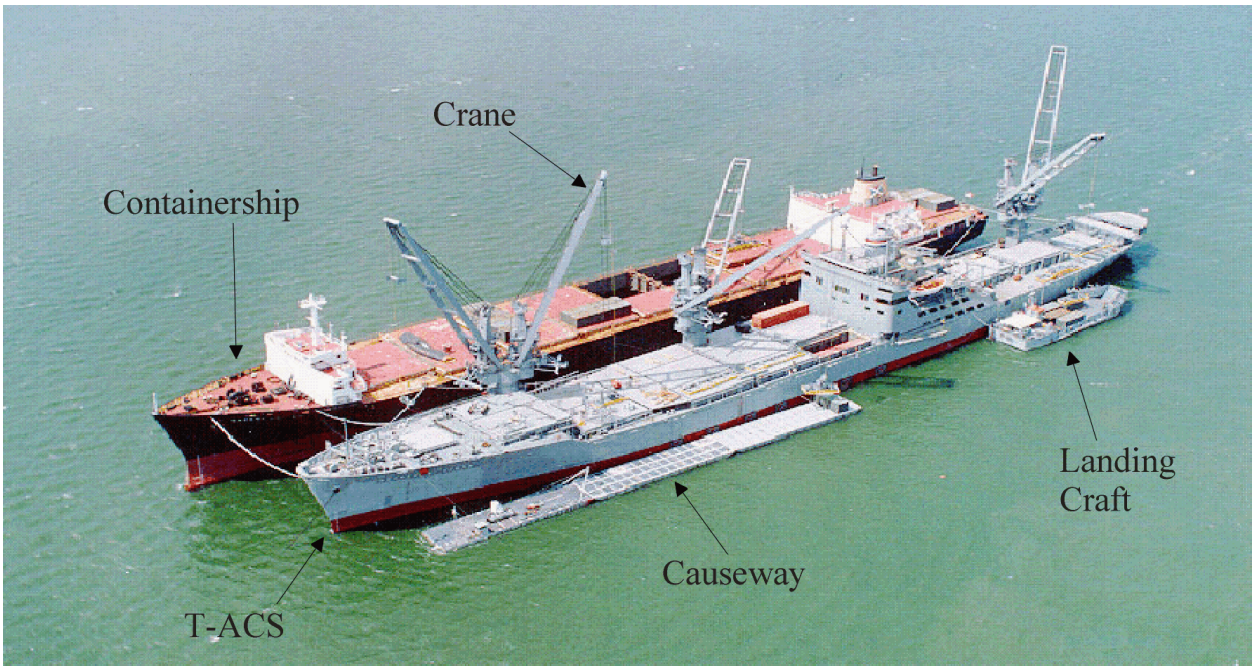

Figure 1.3: Typical T-ACS cargo transfer scenario [5].

caused the cargo hoisted by the T-ACS cranes to begin to swing and operations became difficult and unsafe. In order to achieve sea state 3 LOTS capability, the T-ACS crane must be improved in some way that will suppress load pendulation in rough seas.

1.2 Ship-Mounted Crane Technology

In recent years there has been extensive research into methods of reducing ship-mounted crane load pendulation and improving performance in higher sea states. Several improvements were made to the original design of the T-ACS crane, including the addition of a Rider Block and Tagline System (RBTS). This system, shown in Figure 1.4, is designed to reduce cargo pendulation in rough seas. In this system two taglines restrain the motion of a rider block which is attached to the load hoist cables. The crane operator can control the length of the taglines and the height of the rider block with foot pedals; however, the JLOTS II exercises showed that these controls were rarely used by the operators [3]. Several

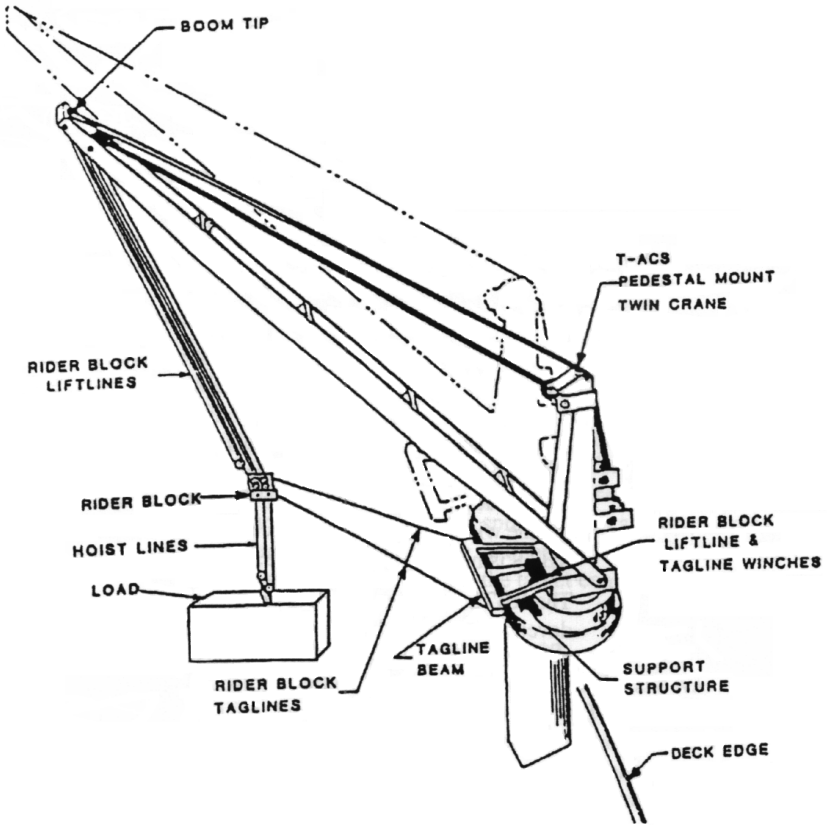

Figure 1.4: Rider Block and Tagline System (RBTS) [3].

other problems were identified during JLOTS II, but the system was able to reduce cargo pendulations to some extent and has since become standard on T-ACS cranes.

Recently, the Integrated Rider Block and Tagline System (IRBTS) was developed as an improvement to the RBTS. The IRBTS coordinates the motion of the rider block and taglines with the motion of the boom as it is raised or lowered. This is done automatically through a computer and therefore eliminates the need for the operator to control the RBTS with the foot pedals. The IRBTS was installed and demonstrated successfully on a T-ACS crane. This system may soon be implemented in the entire fleet.

A device named the Platform Motion Compensator (PMC) was designed to compensate for relative vertical motion between the cargo and lighterage. This system incorporated a second

winch attached to the load hoist cable, which automatically corrected for vertical motion of the cargo due to ship motions. The vertical motion of the cargo was calculated using several sensors including an inertial ship motion sensor. The PMC was tested during JLOTS II exercises and was successful; however it was not installed in the rest of the fleet due to its cost and complexity. [3]

Several other crane architectures and control strategies have been developed over the years, but none of these have been tested or installed on T-ACS cranes. Lacarbonara, Soper, Pratt, Chin, Nayfeh, and Mook investigated the use of Variable Geometry Trusses (VGT) in the suppression of cargo pendulations [3]. These trusses have active members that can change length. They developed the Pendulation Suppression Truss (PST) and the Vibration Isolation Truss (VIT). The VIT would be mounted under the crane and serve to cancel much of the ship motion, while the PST would be mounted at the boom tip and reduce cargo pendulations by pushing or pulling on the load hoist cable. Albus, Bostelman, and Dagalakis [2] at the National Institute of Standards and Technology (NIST) developed the RoboCrane which uses six cables to support the load from the boom. By actuating these cables with winches the cargo can be moved in six degrees of freedom. The Maryland Rigging is a concept developed by Baptista and Hunt where a pulley rides on a cable that is connected to the boom at two different points [3]. The load hoist cable is attached to this pulley. The motion of the pulley can be controlled by changing the friction in the pulley and changing the length of the cable on which it rides. Li and Balachandran investigated the use of mechanical filters to suppress unwanted dynamics of the hoisted cargo [3]. The mechanical filter, which would be suspended from the boom, would contain a cart constrained to move on a concave surface. The load hoist cable would be attached to this cart. Two- and three-dimensional versions as well as active and passive versions of the filter have been investigated theoretically and have proven effective.

1.3 Objective

While the RBTS has shown some success in reducing pendulations, operation of T-ACS cranes is still impossible in sea state 3 and above. Some of the other ideas described above show promise in further suppressing pendulations, but they all require significant modifications to the structure of the crane, which will be costly. Our goal is to reduce crane load pendulations with a minimum of modification to the existing crane design. In order to accomplish this we developed an active control scheme that can be applied to the crane. In this thesis we develop the control algorithm, demonstrate its effectiveness through computer simulations, and then verify these results experimentally using a 1/24th scale model of a T-ACS crane. In order to conduct the experiments, we first needed to design and build a platform capable of simulating the motion of a ship with the model crane attached to it.

Chapter 2

Platform Design and Specifications

2.1 Requirements

The ship-motion simulation platform which we built needed to be capable of reproducing the rigid body motions of a T-ACS or similar ship in a seaway. Since rigid bodies can, in general, move in six degrees of freedom, the platform would ideally have six degrees of freedom as well. The six degrees of freedom of a ship are normally specified as three translations: surge, sway, and heave, and three rotations: roll, pitch, and yaw. After further consideration we decided that the most important degrees of freedom in the excitation of the crane are pitch, roll, and heave, because these generate the most critical motions at the base of the crane. It was decided that the platform must have at least these three degrees of freedom. The platform also needed to be capable of displacements and velocities large enough to simulate ship motion while supporting the weight of a scale model crane. The accuracy of the motion, the size of the machine, and the cost were other factors to consider.

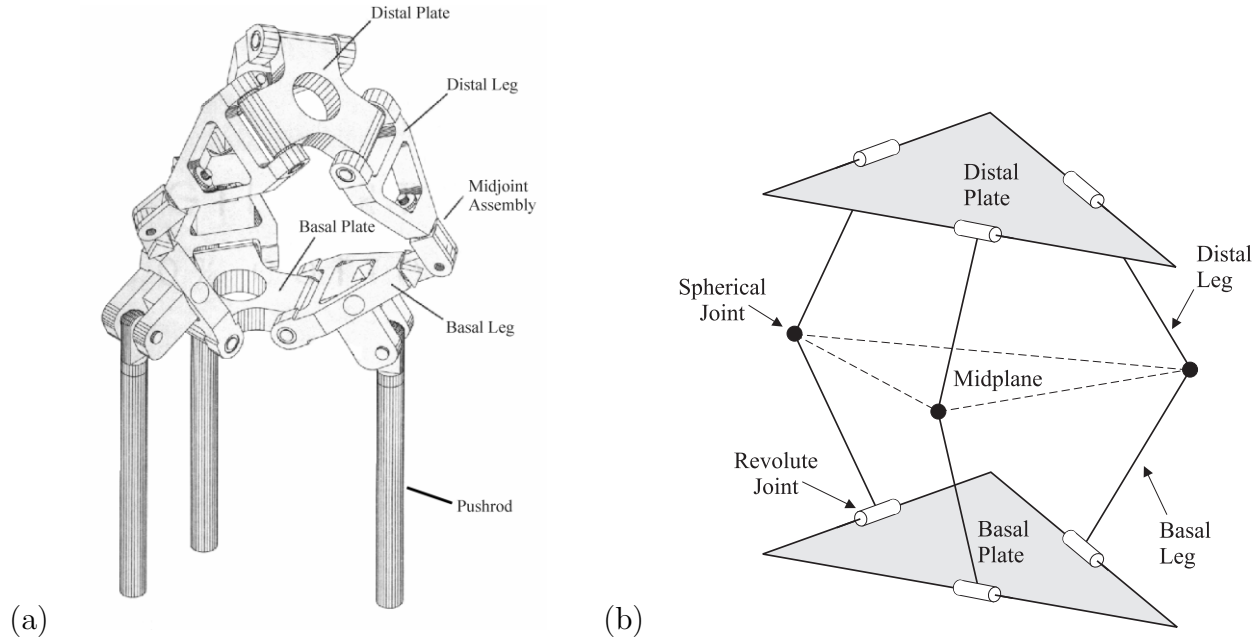

Figure 2.1: (a) shows CAD rendering of Carpal wrist prototype adapted from Ganino [11] and (b) shows a schematic diagram of the structure of the Carpal wrist.

2.2 Architecture

The design we chose is based upon the Carpal wrist, a robotic manipulator developed by Salerno, Ganino, Canfield, and Reinholtz [4, 11, 21]. A CAD rendering of a prototype of the wrist designed by Ganino [11] is shown in Figure 2.1a and a schematic diagram of the robot is shown in Figure 2.1b. The basic structure of the Carpal wrist is symmetric and consists of two plates, the basal plate and the distal plate, connected by three leg pairs. The basal plate is typically rigidly connected to ground or another object. Each plate has three legs connected to it by revolute joints. Each basal leg is connected to the corresponding distal leg with a spherical joint, or equivalently three revolute joints. This configuration allows for the distal plate to move with three degrees of freedom: two rotational degrees of freedom and one translational degree of freedom. The distal plate can be positioned uniquely by specifying the rotation of each basal leg about its revolute joint. In the prototype shown in Figure 2.1a, this is done using the pushrods connected to the basal legs.

The Carpal wrist evolved from a design for a constant-velocity universal joint developed by Clemens in 1872 [7]. Hunt, in 1978, adapted this design for use as a robotic manipulator [12]. Padmanabhan et al. [18] investigated the mechanism and developed an inverse kinematic analysis for it. Salerno et al. [21] further developed closed-form kinematic solutions for the Carpal wrist. Ganino [11] designed and built a proof-of-concept prototype of the Carpal wrist and Canfield [4] furthered the analysis of the robot, including the development of a dynamic analysis.

As its name implies, the Carpal wrist was intended to be used as a robotic *wrist*. Robotic systems are typically divided into two parts: a wrist and an arm. The wrist is attached to the end of the arm and is used to orient a tool fixed to it. The arm, on the other hand, is used to position the wrist and tool. The wrist usually has two or three degrees of freedom and the arm normally has three degrees of freedom, giving the overall robotic system five or six degrees of freedom [9].

One feature of the Carpal wrist which sets it apart from most other robotic wrists is its parallel architecture. A parallel robot has multiple paths from the end effector to ground and some of its joints are passive. The alternative is a serial architecture, where there is a single path to ground and all the joints are active. Most wrists in commercial use today have a serial architecture where the axes of the actuators are orthogonal and intersect at one point. This makes the analysis of the robot simpler. The analysis of parallel robots is generally much more complicated than serial robots and often requires the use of numerical methods to solve the kinematics. This makes online computation, and therefore real-time control, difficult. Another common drawback found in parallel robots is their small workspace. While their truss-like structure often limits their ability to perform large motions, it generally gives parallel robots a much higher strength to weight ratio than their serial counterparts.

The Carpal wrist has several unique features and advantages that make it desirable for use as a ship-motion simulation platform. As mentioned above, the forward and inverse kinematics of the Carpal wrist can be solved in closed-form [21]. Additionally, the Carpal wrist has no

singularities inside its workspace. Singularities, commonly found in both serial and parallel robots, result in the loss of mobility of the robot. Unlike many parallel robots, the Carpal wrist can be designed with a large workspace. The strength of the parallel architecture makes it possible for the Carpal wrist to carry heavy payloads. The open interior allows wires to be run from the basal plate to the distal plate without interference. This feature led to the name of the Carpal wrist since its open interior is similar to the carpal tunnel in the human wrist.

We also considered using a serial robot or a Stewart platform, which is a parallel robot with six degrees of freedom commonly used to provide motion for flight simulators. Both had undesirable features that made them inferior to the Carpal wrist. The Stewart platform has a limited range of motion and more complicated kinematics, and a serial robot would have to be huge to support the weight of a scale model of a crane.

When designing a Carpal wrist there are three important distances that need to be considered. These are the plunge distance, the leg length, and the base length. The plunge distance is the distance from the center of either the distal or basal plate to the center of the wrist. The center of the wrist is defined as the point of intersection of the normal vector passing through the center of the basal plate and the normal vector passing through the center of the distal plate. This point is always located in the midplane, which is defined by the three spherical joints. The leg length is the distance from the center of one revolute joint to the center of the spherical joint on the same leg. The base length is the distance from the center of the basal plate to the center of a basal revolute joint. These distances lead to two kinematic ratios which affect the range of motion of the robot: the plunge ratio R_d and base-to-leg ratio R_b. The plunge ratio is equal to the plunge distance divided by the leg length and the base-to-leg ratio is defined as the base length divided by the leg length. The ship-motion simulation platform was designed with the same kinematic ratios as the Carpal wrist prototype, although the dimensions of the ship-motion simulation platform are four times larger in order to support a larger payload. The ship-motion simulation platform was

designed with $R_b = 0.375$, $R_d = 0.875$, and a base length of 4.724 inches, making the leg length 12.598 inches.

In addition to making the dimensions larger, we did make several other modifications to the design of the Carpal wrist prototype, shown in Figure 2.2a, in order to make it suitable for a ship-motion simulation platform rather than a robotic wrist. The ship-motion simulation platform is shown in Figure 2.2b. The Carpal wrist prototype was designed with long pushrods and support columns in order to keep the motors away from the wrist structure, which is desirable in a robotic wrist. The pushrods were shortened and the support columns were eliminated in the design of the ship-motion simulation platform since there is no reason to keep the actuators away from the rest of the structure. Eliminating these parts also lowered the center of gravity of the robot, making the platform more stable. The tool on the Carpal wrist prototype was replaced by a distal plate extension and cantilever beams, which support the scale model crane and help to simulate rotation about the center of gravity of the ship. The simulated rotation about the center of gravity of the ship will be explained in more detail in Chapter 3 when the kinematics of the platform are discussed.

The Carpal wrist prototype was actuated using rotary stepper motors with 50:1 reduction gearboxes and a four-bar parallel linkage connecting each gearbox to a basal leg. Stepper motors allow open-loop control, thereby eliminating the need for encoders or other feedback devices, and thus reducing cost. The disadvantages of stepper motors are that they can lose track of their position under heavy loads and they are noisy.

We chose to use rotary DC servo motors to actuate our platform. Closed-loop control is necessary with servo motors, and to facilitate this, encoders were used for feedback purposes. Similar to the Carpal wrist prototype, we used reduction gearboxes and a four-bar parallel linkage to transmit the torque from the motors to the basal legs. A non-parallel four-bar linkage could have been used to further increase the torque on the basal legs. We chose the parallel linkage because, while there is no force generated in the linkage, the input-output relationship is linear. This makes the kinematics and control simpler.

(a)

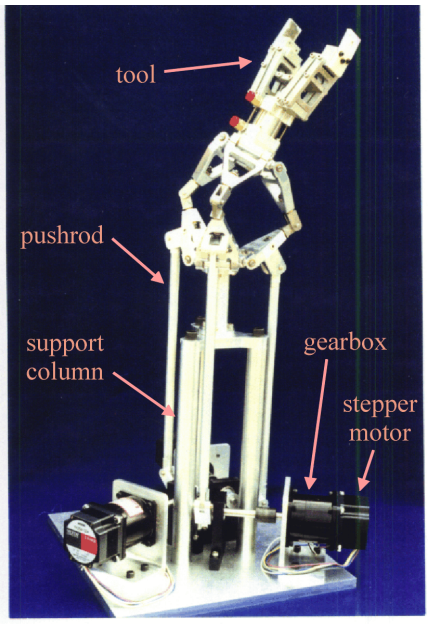

(b)

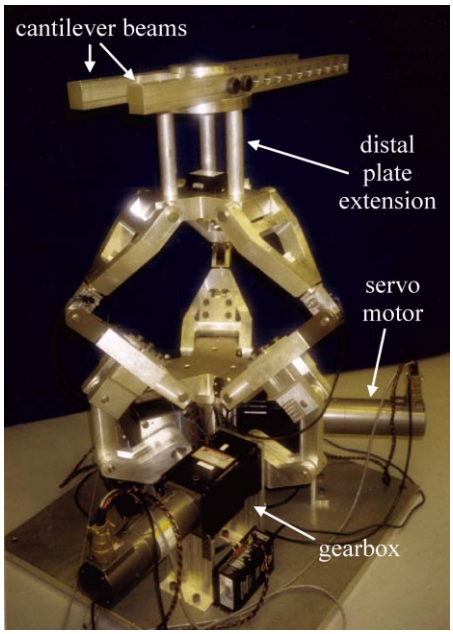

Figure 2.2: Pictures of (a) the Carpal wrist prototype adapted from Ganino [11] and (b) the ship-motion simulation platform.

2.3 Components

Most of the structural members of the platform were machined from aluminum. The only exceptions are the midjoints and all of the pins, which are steel. We chose to use Bayside PG-142-100 Planetary gearheads, which have a 100:1 reduction ratio. The motors used are Baldor MEB-3363 DC servo motors with a continuous torque rating of 11.3 in-lbs and a peak torque of 75 in-lbs. These motors are equipped with 1000 line optical encoders for feedback purposes and a brake to insure that the platform does not move while there is no power to the motors. The amplifiers are Advanced Motion Controls model 50A20 with 25 amps of continuous current and 50 amps peak current. Limit switches were installed to prevent the platform from moving past safe limits and to provide references for calibrating the position of the platform.

2.4 Performance

Quantifying the capabilities of the ship-motion simulation platform is difficult since almost all of the parameters are interdependent. The platform is capable of pitch and roll motions of up to $\pm 20^\circ$ and heave motions of up to ± 6 inches. However, the maximum pitch and roll amplitudes are limited by the heave amplitude since the wrist has less mobility at large plunge ratios. This is illustrated in Figure 2.3. The frequency of the motions is limited by the amplitudes of pitch, roll, and heave. At $\pm 5^\circ$ of pitch and roll and ± 1 inch of heave, the maximum frequencies are about 1 Hz in each pitch, roll, and heave. These maximum frequencies depend on one another. If one frequency was decreased, for example, the other two could be increased. The payload capacity is again dependent on the amplitudes and frequencies of the motions as well as the center of gravity of the payload; however, for reasonable motions, the platform was designed to support a load of over two hundred pounds. Due to the tolerances in the machining of the platform, the accuracy of the platform is again difficult to quantify. The encoders have a resolution of 0.09°. This resolution is increased to 0.0009° due to the 100:1 gearboxes. Unfortunately, this resolution cannot be realized after the gearboxes since the gearboxes have a backlash of approximately 0.17°. Even after adding the errors due to the tolerances in machining to this backlash, it is safe to say that the platform is much more accurate than it needs to be in order to simulate ship motion effectively. The amplitude, frequency, and payload capabilities are also sufficient for the 1/24th scale crane model that was used in our experiments.

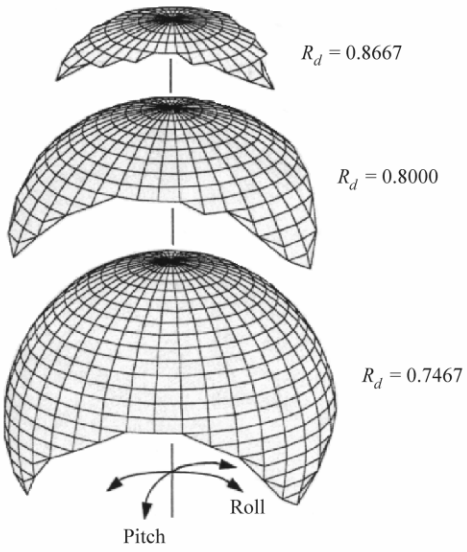

Figure 2.3: Workspace of the Carpal wrist for $R_b = 0.667$ and several values of R_d. Adapted from Ganino [11]

Chapter 3

Platform Kinematics

3.1 Modeling Ship Motion

In order to accurately simulate the motion of the ship, we must first determine the kinematics between the ship and the motors. The first step is to specify the rigid body motion of the ship with respect to an inertially fixed coordinate system. This motion can be divided into two types: rotational motion and translational motion. It is conventional to specify the rotational motion using three angles: roll, pitch, and yaw. The translational motion is normally specified using three displacements: surge, sway, and heave.

As shown in Figure 3.1, we define a body-fixed coordinate system D, which, in general, is not located at the center of mass of the ship. We also define an earth-fixed system B, which can be considered inertially fixed for this problem. Following the notation in Fossen [10], we specify the rigid-body orientation of the ship using the Euler angles ϕ, θ, and ψ, where ϕ is the roll angle, θ is the pitch angle, and ψ is the yaw angle. The translation of the ship is described by the linear displacements x, y, and z, which represent surge, sway, and heave, respectively. The linear and angular position of the ship is measured in the inertially fixed B

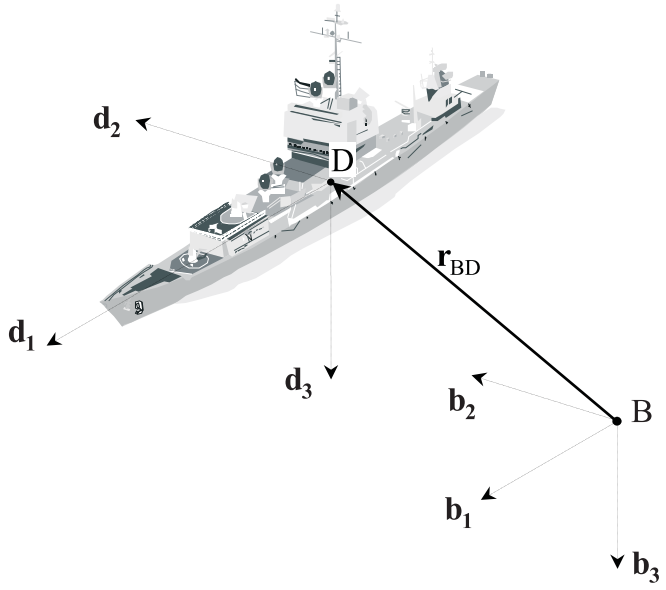

Figure 3.1: Earth-fixed and body-fixed coordinate systems.

frame. Surge is measured along the $\mathbf{b_1}$ axis, sway is measured along the $\mathbf{b_2}$ axis, and heave is measured along the $\mathbf{b_3}$ axis. The velocity of the ship is specified using six components. The roll rate is p, the pitch rate is q, and the yaw rate is r, while the surge, sway, and heave rates are u, v, and w, respectively. All velocities are measured in the body-fixed D frame. The distal frame is oriented so that p and u are measured along the $\mathbf{d_1}$ axis, q and v are measured along the $\mathbf{d_2}$ axis, and r and w are measured along the $\mathbf{d_3}$ axis.

When simulating the ship motion with the platform, one can think of the distal plate of the platform to be analogous to the ship and the basal plate to be analogous to the earth. Therefore, we fix the D coordinate system to the distal plate and the B coordinate system to the basal plate.

3.2 Rotation

We use a 3-2-1 set of Euler angles to describe the orientation of the ship relative to the earth. Starting with the B and D coordinate systems aligned, we rotate the distal plate an angle ψ

about $\mathbf{b_3}$ to an intermediate coordinate system A. Next we rotate it an angle θ about $\mathbf{a_2}$ to another intermediate coordinate system C. Finally, we rotate it an angle ϕ about the axis $\mathbf{c_1}$ to reach the body-fixed coordinate system D. Writing this in matrix form, we have

$$\mathbf{d} = \begin{bmatrix} 1 & 0 & 0 \\ 0 & c\phi & s\phi \\ 0 & -s\phi & c\phi \end{bmatrix} \begin{bmatrix} c\theta & 0 & -s\theta \\ 0 & 1 & 0 \\ s\theta & 0 & c\theta \end{bmatrix} \begin{bmatrix} c\psi & s\psi & 0 \\ -s\psi & c\psi & 0 \\ 0 & 0 & 1 \end{bmatrix} \mathbf{b} \tag{3.1}$$

where $\mathbf{b}$ and $\mathbf{d}$ are vectors of the base vectors of the B and D coordinate systems, respectively. We obtain the rotation matrix by multiplying the three simple rotation matrices in Eq. (3.1) together. The result is

$$\mathbf{d} = \begin{bmatrix} c\theta c\psi & c\theta s\psi & -s\theta \\ c\psi s\theta s\phi - c\phi s\psi & c\phi c\psi + s\theta s\phi s\psi & c\theta s\phi \\ c\phi c\psi s\theta + s\phi s\psi & -c\psi s\phi + c\phi s\theta s\psi & c\theta c\phi \end{bmatrix} \mathbf{b} \tag{3.2}$$

Now we need to develop the rate kinematics between the two coordinate systems. The angular velocity of coordinate system D with respect to coordinate system B is

$${}^{B}\omega^{D} = \dot{\psi}\mathbf{a_3} + \dot{\theta}\mathbf{c_2} + \dot{\phi}\mathbf{d_1} \tag{3.3}$$

The $\mathbf{a_3}$ and $\mathbf{c_2}$ unit vectors can be expressed in terms of the base vectors of the D coordinate system:

$$\mathbf{a_3} = -\sin\theta\mathbf{d_1} + \sin\phi\cos\theta\mathbf{d_2} + \cos\phi\cos\theta\mathbf{d_3} \tag{3.4}$$

$$\mathbf{c_2} = \cos\phi\mathbf{d_2} - \sin\phi\mathbf{d_3} \tag{3.5}$$

Substituting Eqs. (3.4) and (3.5) into Eq. (3.3) and gathering terms we obtain

$$ {}^{B}\omega^{D} = (\dot{\phi} - \dot{\psi}\sin\theta)\mathbf{d_1} + (\dot{\psi}\sin\phi\cos\theta + \dot{\theta}\cos\phi)\mathbf{d_2} + (\dot{\psi}\cos\phi\cos\theta - \dot{\theta}\sin\phi)\mathbf{d_3} \tag{3.6} $$

Rewriting Eq. (3.6) in matrix form and using the fact that p, q, and r are the components of the angular velocities in frame D, we obtain the forward rate kinematics:

$$ \begin{pmatrix} p \\ q \\ r \end{pmatrix} = \begin{bmatrix} -\sin\theta & 0 & 1 \\ \sin\phi\cos\theta & \cos\phi & 0 \\ \cos\phi\cos\theta & -\sin\phi & 0 \end{bmatrix} \begin{pmatrix} \dot{\psi} \\ \dot{\theta} \\ \dot{\phi} \end{pmatrix} \tag{3.7} $$

We can find the inverse rate kinematics by simply inverting Eq. (3.7):

$$ \begin{pmatrix} \dot{\psi} \\ \dot{\theta} \\ \dot{\phi} \end{pmatrix} = \frac{1}{\cos\theta} \begin{bmatrix} 0 & \sin\phi & \cos\phi \\ 0 & \cos\phi\cos\theta & -\sin\phi\cos\theta \\ \cos\theta & \sin\phi\sin\theta & \cos\phi\sin\theta \end{bmatrix} \begin{pmatrix} p \\ q \\ r \end{pmatrix} \tag{3.8} $$

We see that a singularity exists at $\theta = \pm 90^{\circ}$, but this condition cannot be physically reached without capsizing the ship. We must integrate Eq. (3.8) to find the Euler angles as functions of time.

3.3 Perturbation Solution

If the angular rates are sinusoidal and lead to small angular displacements, we can find approximate analytic solutions for the Euler angles using a straightforward expansion [13].

Let us assume that the roll, pitch, and yaw rates are given by

$$\begin{aligned} p &= A_1\Omega_1 \cos\Omega_1 t \\ q &= A_2\Omega_2 \cos\Omega_2 t \\ r &= 0 \end{aligned} \tag{3.9}$$

We set the yaw rate equal to zero in Eqs. (3.9) since the platform is not capable of performing this motion.

We expand Eq. (3.8) in a Taylor series about $\phi = \theta = \psi = 0$, keep terms up to third order, and obtain

$$\begin{aligned} \dot{\psi} &= r + q\phi + \frac{1}{2}r\theta^2 - \frac{1}{2}r\phi^2 \\ \dot{\theta} &= q - r\phi - \frac{1}{2}q\phi^2 \\ \dot{\phi} &= p + r\theta + q\theta\phi \end{aligned} \tag{3.10}$$

Substituting Eqs. (3.9) into Eqs. (3.10) and specifying that the coordinate systems are aligned at $t = 0$, we have

$$\begin{aligned} \dot{\psi} &= A_2\Omega_2\phi\cos\Omega_2 t & \psi(0) &= 0 \\ \dot{\theta} &= A_2\Omega_2\cos\Omega_2 t - \frac{1}{2}A_2\Omega_2\phi^2\cos\Omega_2 t & \theta(0) &= 0 \\ \dot{\phi} &= A_1\Omega_1\cos\Omega_1 t + A_2\Omega_2\theta\phi\cos\Omega_2 t & \phi(0) &= 0 \end{aligned} \tag{3.11}$$

We introduce a bookkeeping parameter ϵ and let

$$\begin{aligned} A_1 &= \epsilon A_1 \\ A_2 &= \epsilon A_2 \end{aligned} \tag{3.12}$$

Now we assume a solution in the form

$$\begin{aligned}\psi(t;\epsilon) &= \epsilon\psi_1(t) + \epsilon^2\psi_2(t) + \epsilon^3\psi_3(t) + \dots \\ \theta(t;\epsilon) &= \epsilon\theta_1(t) + \epsilon^2\theta_2(t) + \epsilon^3\theta_3(t) + \dots \\ \phi(t;\epsilon) &= \epsilon\phi_1(t) + \epsilon^2\phi_2(t) + \epsilon^3\phi_3(t) + \dots\end{aligned} \tag{3.13}$$

Substituting Eqs. (3.12) and (3.13) into Eqs. (3.11) we obtain

$$\begin{aligned}\epsilon\dot{\psi}_1 + \epsilon^2\dot{\psi}_2 + \epsilon^3\dot{\psi}_3 &= \epsilon^2\phi_1 A_2\Omega_2\cos\Omega_2 t + \epsilon^3\phi_2 A_2\Omega_2\cos\Omega_2 t \\ \epsilon\dot{\theta}_1 + \epsilon^2\dot{\theta}_2 + \epsilon^3\dot{\theta}_3 &= \epsilon A_2\Omega_2\cos\Omega_2 t - \epsilon^3\frac{1}{2}\phi_1^2 A_2\Omega_2\cos\Omega_2 t \\ \epsilon\dot{\phi}_1 + \epsilon^2\dot{\phi}_2 + \epsilon^3\dot{\phi}_3 &= \epsilon A_1\Omega_1\cos\Omega_1 t + \epsilon^3\phi_1\theta_1 A_2\Omega_2\cos\Omega_2 t\end{aligned} \tag{3.14}$$

Equating coefficients of like powers of ϵ yields

$$\begin{aligned}\text{Order } \epsilon^1: \quad \dot{\psi}_1 &= 0 \\ \dot{\theta}_1 &= A_2\Omega_2\cos\Omega_2 t \\ \dot{\phi}_1 &= A_1\Omega_1\cos\Omega_1 t\end{aligned} \tag{3.15}$$

$$\begin{aligned}\text{Order } \epsilon^2: \quad \dot{\psi}_2 &= \phi_1 A_2\Omega_2\cos\Omega_2 t \\ \dot{\theta}_2 &= 0 \\ \dot{\phi}_2 &= 0\end{aligned} \tag{3.16}$$

and

$$\begin{aligned}\text{Order } \epsilon^3: \quad \dot{\psi}_3 &= \phi_2 A_2\Omega_2\cos\Omega_2 t \\ \dot{\theta}_3 &= -\frac{1}{2}\phi_1^2 A_2\Omega_2\cos\Omega_2 t \\ \dot{\phi}_3 &= \theta_1\phi_1 A_2\Omega_2\cos\Omega_2 t\end{aligned} \tag{3.17}$$

The first-order solution is

$$\begin{aligned} \psi_1 &= C_1 \\ \theta_1 &= C_2 + A_2 \sin \Omega_2 t \\ \phi_1 &= C_3 + A_1 \sin \Omega_1 t \end{aligned} \tag{3.18}$$

Now we substitute Eqs. (3.18) into Eqs. (3.16) and obtain

$$\begin{aligned} \dot{\psi}_2 &= (C_3 + A_1 \sin \Omega_1 t) A_2 \Omega_2 \cos \Omega_2 t \\ \dot{\theta}_2 &= 0 \\ \dot{\phi}_2 &= 0 \end{aligned} \tag{3.19}$$

The particular solution of the last two of Eqs. (3.19) is

$$\begin{aligned} \theta_2 &= 0 \\ \phi_2 &= 0 \end{aligned} \tag{3.20}$$

The first of Eqs. (3.19) can be rewritten as

$$\dot{\psi}_2 = C_3 A_2 \Omega_2 \cos \Omega_2 t + \frac{1}{2} A_1 A_2 \Omega_2 \{\sin[(\Omega_1 - \Omega_2)t] + \sin[(\Omega_1 + \Omega_2)t]\} \tag{3.21}$$

There are two cases that should be considered: $\Omega_1 = \Omega_2$, and $\Omega_1 \neq \Omega_2$. For the case $\Omega_1 = \Omega_2$, Eq. (3.21) reduces to

$$\dot{\psi}_2 = C_3 A_2 \Omega_2 \cos \Omega_2 t + \frac{1}{2} A_1 A_2 \Omega_2 \sin(2\Omega_2 t) \tag{3.22}$$

The solution of Eq. (3.22) is

$$\psi_2 = A_2 C_3 \sin \Omega_2 t - \frac{1}{4} A_1 A_2 \cos(2\Omega_2 t) \tag{3.23}$$

For the case $\Omega_1 \neq \Omega_2$, the solution of Eq. (3.21) is

$$\psi_2 = C_3 A_2 \sin\Omega_2 t - \frac{A_1 A_2 \Omega_2}{2(\Omega_1+\Omega_2)}\cos[(\Omega_1+\Omega_2)t] - \frac{A_1 A_2 \Omega_2}{2(\Omega_1-\Omega_2)}\cos[(\Omega_1-\Omega_2)t] \tag{3.24}$$

In either case the third-order equations become

$$\begin{aligned}
\dot{\psi}_3 &= 0 \\
\dot{\theta}_3 &= -\frac{1}{4}A_1^2 A_2 \Omega_2 \cos\Omega_2 t - \frac{1}{2}C_3^2 A_2 \Omega_2 \cos\Omega_2 t \\
&\quad + \frac{1}{8}A_1^2 A_2 \Omega_2 \cos[(2\Omega_1-\Omega_2)t] + \frac{1}{8}A_1^2 A_2 \Omega_2 \cos[(2\Omega_1+\Omega_2)t] \\
&\quad - \frac{1}{2}C_3 A_1 A_2 \Omega_2 \sin[(\Omega_1-\Omega_2)t] - \frac{1}{2}C_3 A_1 A_2 \Omega_2 \sin[(\Omega_1+\Omega_2)t] \\
\dot{\phi}_3 &= C_2 C_3 A_2 \Omega_2 \cos\Omega_2 t + \frac{1}{4}A_1 A_2^2 \Omega_2 \cos[(\Omega_1-2\Omega_2)t] \\
&\quad - \frac{1}{4}A_1 A_2^2 \Omega_2 \cos[(\Omega_1+2\Omega_2)t] + \frac{1}{2}C_3 A_2^2 \Omega_2 \sin 2\Omega_2 t \\
&\quad + \frac{1}{2}C_2 A_1 A_2 \Omega_2 \sin[(\Omega_1-\Omega_2)t] + \frac{1}{2}C_2 A_1 A_2 \Omega_2 \sin[(\Omega_1+\Omega_2)t]
\end{aligned} \tag{3.25}$$

We must consider four cases here: $\Omega_1 = \frac{1}{2}\Omega_2$, $\Omega_1 = \Omega_2$, $\Omega_1 = 2\Omega_2$, and $\Omega_1 \neq \frac{1}{2}\Omega_2$, Ω_2, or $2\Omega_2$. For $\Omega_1 = \frac{1}{2}\Omega_2$, the third-order particular solution is

$$\begin{aligned}
\psi_3 &= 0 \\
\theta_3 &= -\frac{1}{4}A_1^2 A_2 \sin\Omega_2 t - \frac{1}{2}C_3^2 A_2 \sin\Omega_2 t + \frac{1}{8}A_1^2 A_2 \Omega_2 t \\
&\quad + \frac{1}{16}A_1^2 A_2 \sin 2\Omega_2 t - C_3 A_1 A_2 \cos\frac{\Omega_2}{2}t + \frac{1}{3}C_3 A_1 A_2 \cos\frac{3\Omega_2}{2}t \\
\phi_3 &= C_2 C_3 A_2 \sin\Omega_2 t + \frac{1}{6}A_1 A_2^2 \sin\frac{3\Omega_2}{2}t - \frac{1}{10}A_1 A_2^2 \sin\frac{5\Omega_2}{2}t \\
&\quad - \frac{1}{4}C_3 A_2^2 \cos 2\Omega_2 t + C_2 A_1 A_2 \cos\frac{\Omega_2}{2}t - \frac{1}{3}C_2 A_1 A_2 \cos\frac{3\Omega_2}{2}t
\end{aligned} \tag{3.26}$$

Substituting Eqs. (3.18), (3.20), (3.24), and (3.26) into Eqs. (3.13) and setting $\epsilon = 1$ yields

$$\begin{aligned}
\psi &= C_1 + A_1 A_2 \cos\frac{\Omega_2}{2}t - \frac{1}{3}A_1 A_2 \cos\frac{3\Omega_2}{2}t + C_3 A_2 \sin\Omega_2 t \\
\theta &= C_2 + A_2 \sin\Omega_2 t + \frac{1}{8}A_1^2 A_2 \Omega_2 t - C_3 A_1 A_2 \cos\frac{\Omega_2}{2}t + \frac{1}{3}C_3 A_1 A_2 \cos\frac{3\Omega_2}{2}t \\
&\quad - \frac{1}{4}A_1^2 A_2 \sin\Omega_2 t - \frac{1}{2}C_3^2 A_2 \sin\Omega_2 t + \frac{1}{16}A_1^2 A_2 \sin 2\Omega_2 t \\
\phi &= C_3 + A_1 \sin\frac{\Omega_2}{2}t + C_2 A_1 A_2 \cos\frac{\Omega_2}{2}t - \frac{1}{3}C_2 A_1 A_2 \cos\frac{3\Omega_2}{2}t \\
&\quad - \frac{1}{4}C_3 A_2^2 \cos 2\Omega_2 t + C_2 C_3 A_2 \sin\Omega_2 t + \frac{1}{6}A_1 A_2^2 \sin\frac{3\Omega_2}{2}t - \frac{1}{10}A_1 A_2^2 \sin\frac{5\Omega_2}{2}t
\end{aligned} \tag{3.27}$$

Now we can solve for the constants by applying the initial conditions to the equations above. The constants are

$$\begin{aligned}
C_1 &= -\frac{2}{3}A_1 A_2 \\
C_2 &= 0 \\
C_3 &= 0
\end{aligned} \tag{3.28}$$

Substituting these constants into Eqs. (3.27) we obtain the following solution:

$$\begin{aligned}
\psi &= -\frac{2}{3}A_1 A_2 + A_1 A_2 \cos\frac{\Omega_2}{2}t - \frac{1}{3}A_1 A_2 \cos\frac{3\Omega_2}{2}t \\
\theta &= A_2 \sin\Omega_2 t + \frac{1}{8}A_1^2 A_2 \Omega_2 t - \frac{1}{4}A_1^2 A_2 \sin\Omega_2 t + \frac{1}{16}A_1^2 A_2 \sin 2\Omega_2 t \\
\phi &= A_1 \sin\frac{\Omega_2}{2}t + \frac{1}{6}A_1 A_2^2 \sin\frac{3\Omega_2}{2}t - \frac{1}{10}A_1 A_2^2 \sin\frac{5\Omega_2}{2}t
\end{aligned} \tag{3.29}$$

For the case $\Omega_1 = \Omega_2$, the third-order particular solution is

$$\begin{aligned}
\psi_3 &= 0 \\
\theta_3 &= -\frac{1}{4}A_1^2 A_2 \sin\Omega_2 t - \frac{1}{2}C_3^2 A_2 \sin\Omega_2 t + \frac{1}{8}A_1^2 A_2 \sin\Omega_2 t \\
&\quad + \frac{1}{24}A_1^2 A_2 \sin 3\Omega_2 t + \frac{1}{4}C_3 A_1 A_2 \cos 2\Omega_2 t \\
\phi_3 &= C_2 C_3 A_2 \sin\Omega_2 t + \frac{1}{4}A_1 A_2^2 \sin\Omega_2 t - \frac{1}{12}A_1 A_2^2 \sin 3\Omega_2 t \\
&\quad - \frac{1}{4}C_3 A_2^2 \cos 2\Omega_2 t - C_2 A_1 A_2 \cos 2\Omega_2 t
\end{aligned} \tag{3.30}$$

Substituting the first, second, and third-order solutions into Eqs. (3.13), setting $\epsilon = 1$, and solving for the constants of integration, we find that the solution for the case $\Omega_1 = \Omega_2$ is

$$\begin{aligned}
\psi &= \frac{1}{4}A_1 A_2 - \frac{1}{4}A_1 A_2 \cos 2\Omega_2 t \\
\theta &= A_2 \sin\Omega_2 t - \frac{1}{8}A_1^2 A_2 \sin\Omega_2 t + \frac{1}{3}A_1^2 A_2 \sin 3\Omega_2 t \\
\phi &= A_1 \sin\Omega_2 t + \frac{1}{4}A_1 A_2^2 \sin\Omega_2 t - \frac{1}{3}A_1 A_2^2 \sin 3\Omega_2 t
\end{aligned} \tag{3.31}$$

For the case $\Omega_1 = 2\Omega_2$, the third-order particular solution is

$$\begin{aligned}
\psi_3 &= 0 \\
\theta_3 &= -\frac{1}{4}A_1^2 A_2 \sin\Omega_2 t - \frac{1}{2}C_3^2 A_2 \sin\Omega_2 t + \frac{1}{24}A_1^2 A_2 \sin 3\Omega_2 t \\
&\quad + \frac{1}{40}A_1^2 A_2 \sin 5\Omega_2 t + \frac{1}{2}C_3 A_1 A_2 \cos\Omega_2 t + \frac{1}{6}C_3 A_1 A_2 \cos 3\Omega_2 t \\
\phi_3 &= C_2 C_3 A_2 \sin\Omega_2 t + \frac{1}{4}A_1 A_2^2 \Omega_2 t - \frac{1}{16}A_1 A_2^2 \sin 4\Omega_2 t \\
&\quad - \frac{1}{4}C_3 A_2^2 \cos 2\Omega_2 t - \frac{1}{2}C_2 A_1 A_2 \cos\Omega_2 t - \frac{1}{6}C_2 A_1 A_2 \cos 3\Omega_2 t
\end{aligned} \tag{3.32}$$

Following the same procedure as in the first and second cases, we find the solution for the

case $\Omega_1 = 2\Omega_2$:

$$\begin{aligned}
\psi &= \frac{2}{3}A_1A_2 - \frac{1}{2}A_1A_2\cos\Omega_2 t - \frac{1}{6}A_1A_2\cos 3\Omega_2 t \\
\theta &= A_2\sin\Omega_2 t - \frac{1}{4}A_1^2A_2\sin\Omega_2 t + \frac{1}{24}A_1^2A_2\sin 3\Omega_2 t + \frac{1}{40}A_1^2A_2\sin 5\Omega_2 t \\
\phi &= A_1\sin 2\Omega_2 t + \frac{1}{4}A_1A_2^2\Omega_2 t - \frac{1}{16}A_1A_2^2\sin 4\Omega_2 t
\end{aligned} \tag{3.33}$$

Finally, for the case $\Omega_1 \neq \frac{1}{2}\Omega_2$, Ω_2, or $2\Omega_2$, the third-order particular solution is

$$\begin{aligned}
\psi_3 &= 0 \\
\theta_3 &= -\frac{1}{4}A_1^2A_2\sin\Omega_2 t - \frac{1}{2}C_3^2A_2\sin\Omega_2 t + \frac{A_1^2A_2\Omega_2}{8(2\Omega_1-\Omega_2)}\sin[(2\Omega_1-\Omega_2)t] \\
&\quad + \frac{A_1^2A_2\Omega_2}{8(2\Omega_1+\Omega_2)}\sin[(2\Omega_1+\Omega_2)t] + \frac{C_3A_1A_2\Omega_2}{2(\Omega_1-\Omega_2)}\cos[(\Omega_1-\Omega_2)t] \\
&\quad + \frac{C_3A_1A_2\Omega_2}{2(\Omega_1+\Omega_2)}\cos[(\Omega_1+\Omega_2)t] \\
\phi_3 &= C_2C_3A_2\sin\Omega_2 t + \frac{A_1A_2^2\Omega_2}{4(\Omega_1-2\Omega_2)}\sin[(\Omega_1-2\Omega_2)t] \\
&\quad - \frac{A_1A_2^2\Omega_2}{4(\Omega_1+2\Omega_2)}\sin[(\Omega_1+2\Omega_2)t] - \frac{1}{4}C_3A_2^2\cos 2\Omega_2 t \\
&\quad - \frac{C_2A_1A_2\Omega_2}{2(\Omega_1-\Omega_2)}\cos[(\Omega_1-\Omega_2)t] - \frac{C_2A_1A_2\Omega_2}{2(\Omega_1+\Omega_2)}\cos[(\Omega_1+\Omega_2)t]
\end{aligned} \tag{3.34}$$

Once again, following the same procedure as above, the solution for the case $\Omega_1 \neq \frac{1}{2}\Omega_2$, Ω_2,

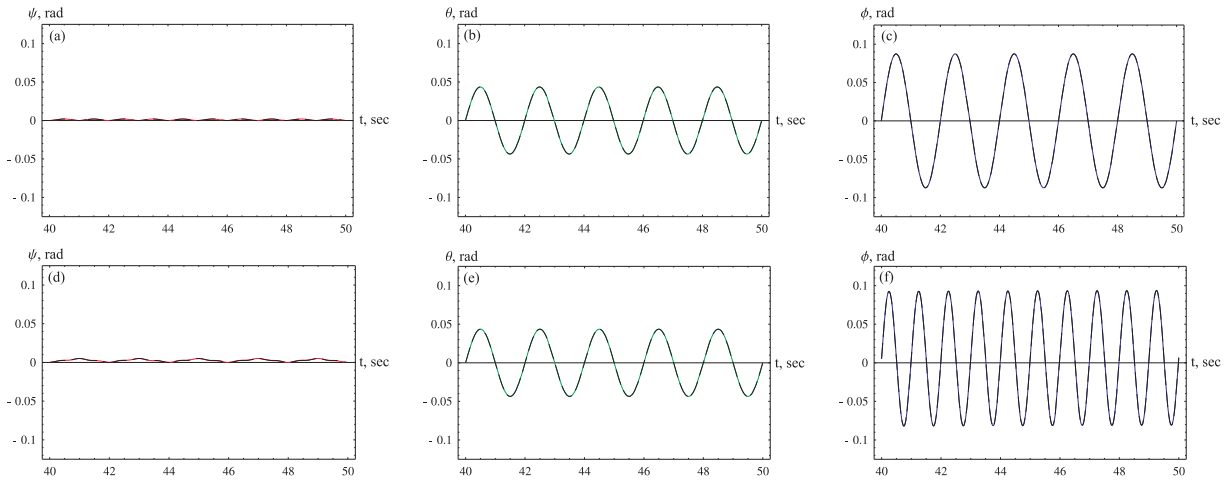

Figure 3.2: Comparison of numerical and analytic Euler angle solutions. The case $\Omega_1 = \Omega_2$ is shown in plots (a), (b), and (c), while (d), (e), and (f) are for $\Omega_1 = 2\Omega_2$. Dashed lines are the approximate analytic solution and the solid lines are the numerical solution.

or $2\Omega_2$ is

$$\begin{aligned}
\psi &= \frac{A_1 A_2 \Omega_1 \Omega_2}{(\Omega_1 - \Omega_2)(\Omega_1 + \Omega_2)} - \frac{A_1 A_2 \Omega_2}{2(\Omega_1 - \Omega_2)} \cos[(\Omega_1 - \Omega_2)t] \\
&\quad - \frac{A_1 A_2 \Omega_2}{2(\Omega_1 + \Omega_2)} \cos[(\Omega_1 + \Omega_2)t] \\
\theta &= A_2 \sin \Omega_2 t - \frac{1}{4} A_1^2 A_2 \sin \Omega_2 t + \frac{A_1^2 A_2 \Omega_2}{8(2\Omega_1 - \Omega_2)} \sin[(2\Omega_1 - \Omega_2)t] \\
&\quad + \frac{A_1^2 A_2 \Omega_2}{8(2\Omega_1 + \Omega_2)} \sin[(2\Omega_1 + \Omega_2)t] \\
\phi &= A_1 \sin \Omega_1 t + \frac{A_1 A_2^2 \Omega_2}{4(\Omega_1 - 2\Omega_2)} \sin[(\Omega_1 - 2\Omega_2)t] - \frac{A_1 A_2^2 \Omega_2}{4(\Omega_1 + 2\Omega_2)} \sin[(\Omega_1 + 2\Omega_2)t]
\end{aligned} \tag{3.35}$$

We can substitute Eqs. (3.9) into Eq. (3.8), numerically integrate, and compare the results to our analytic solutions in order to check the accuracy of our solutions. Figure 3.2 shows the comparison of the numerical solutions to the analytic solutions. The case $\Omega_1 = \Omega_2 = 0.5$ Hz is shown in plots (a), (b), and (c), while the case $\Omega_1 = 2\Omega_2 = 1$ Hz is shown in (d), (e), and (f). The amplitudes are $A_1 = 5.0°$ and $A_2 = 2.5°$ in both cases. Dashed lines are the approximate analytic solution and the solid lines are the numerical solution. In both cases the difference between the two solutions is not visible.

Depending on the ratio between the frequencies of the body-fixed angular velocities, we can substitute the solutions in Eqs. (3.29), (3.31), (3.33), or (3.35) into the rotation matrix in Eq. (3.2) and obtain the orientation of the D coordinate frame as a function of time for sinusoidal roll and pitch rates. This is advantageous if we want to make online calculations.

3.4 Other Methods

For more complicated roll and pitch rate functions, we may not necessarily be able to find a good analytic approximation. In this case we could resort to numerically integrating Eq. (3.8). This may have to be done off-line since numerical integration would require more CPU time than the closed-form solutions.

Finally, we may want to use discrete data for our roll and pitch rates. Such data could be the output from computer simulations of ship motion or data from real ships. In this case we could simply solve Eq. (3.8) at each time step and generate a table of the Euler angle values at each time step.

3.5 Translation

The next step is to determine the correct translation of the origin of the D coordinate frame. In terms of the platform, this means we need to find the plunge distance as a function of time. The plunge distance will depend on the heave, the rotation matrix, and the location of the center of gravity of the ship.

Figure 3.3a shows a schematic diagram of the carpal wrist. We start with the coordinate systems B and D having the same orientation. Point G is the simulated center of gravity of the ship. The location of this point can be calculated by multiplying the dimensions of the actual ship by the scale ratio of the model crane. The distal plate extension was designed to

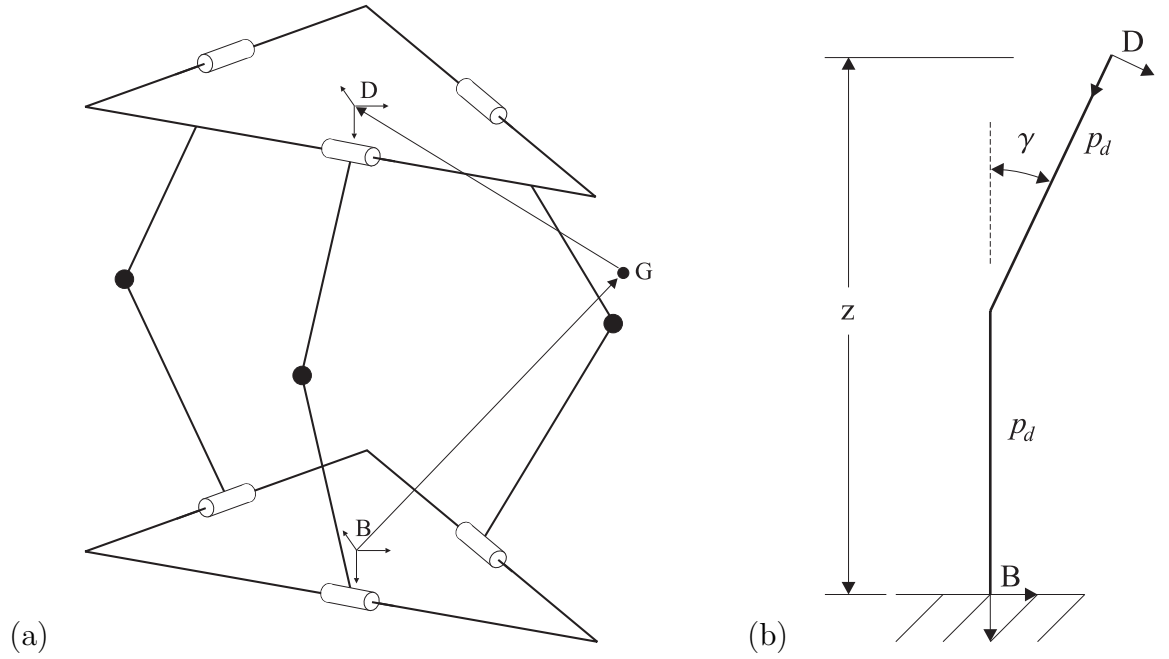

Figure 3.3: Schematic diagrams of the platform: (a) shows a 3D representation of the platform while (b) shows 2D projection.

increase the vertical distance between the crane and the initial midplane of the wrist so that the center of gravity could be located in the initial midplane at the start of the simulation. The cantilever beams mentioned in Chapter 2 can be adjusted to change the location of the crane relative to the distal plate in the horizontal plane. Thus, they allow more freedom in the choice of the location of the simulated center of gravity.

A vector $\mathbf{BG} = (G_x, G_y, -p_d(0) - h(t))$ locates the simulated center of gravity with respect to the B coordinate system, where $p_d(0)$ is the initial plunge distance and $h(t)$ is the heave. The vector $\mathbf{GD}' = (-G_x, -G_y, -p_d(0))$ locates initial position of the origin of the D coordinate system with respect to the simulated center of gravity. Multiplying by the rotation matrix gives us the vector locating the origin of the D coordinate system with respect to the simulated center of gravity at any time:

$$\mathbf{GD} = [\mathbf{R}]\ \mathbf{GD}' \tag{3.36}$$

Adding the negative of the z components of the **BG** and the **GD** vectors, we find the height of the origin of the D coordinate frame above the basal plate:

$$z(t) = p_d(0) + h(t) - \mathbf{GD} \cdot \mathbf{b_3} \tag{3.37}$$

Now that $z(t)$ is known, we can find the plunge distance as a function of time. As shown in Figure 3.3b, the platform can be represented schematically as two links connected by a spherical joint at the center of the wrist. Examining this model, we see that

$$z(t) = p_d(t) + p_d(t) \cos\gamma \tag{3.38}$$

Since we know that

$$\cos\gamma = (\mathbf{b_3} \cdot \mathbf{d_3}) \tag{3.39}$$

Eq (3.38) can be rewritten as

$$z(t) = p_d(t) + p_d(t)(\mathbf{b_3} \cdot \mathbf{d_3}) \tag{3.40}$$

Solving for the plunge distance, we find

$$p_d(t) = \frac{z(t)}{1 + \mathbf{b_3} \cdot \mathbf{d_3}} \tag{3.41}$$

While this plunge distance will produce the correct heave motion of the platform, it may introduce small sway and surge motions as well. This is due to the fact that for $\gamma \neq 0$, the platform does not move purely in the negative $\mathbf{b_3}$ direction as we increase the heave. However, the surge and sway motions will be very small for small values of γ.

Knowledge of the rotation matrix and plunge distance as functions of time is sufficient to continue with the kinematics developed in Ganino [11]. These kinematics determine the

angles of the three input links of the four bar linkages required to produce a given rotation matrix and plunge distance. Once these three angles are found we can move on to the control of the platform.

Chapter 4

Platform Control

4.1 Controller Selection

We must now develop an algorithm which controls the positions of the motor shafts according to the desired input link angles found with the inverse kinematics. As mentioned in Chapter 2 this must be a closed-loop (or feedback) control system since we are using DC servo motors.

Control systems are generally divided into two categories: regulators and servomechanisms [19]. Regulators attempt to maintain a constant value of the controlled variable while servomechanisms attempt to track a reference signal which is changing with time [19]. Since each of the three desired motor positions will, in general, be changing with time we will need to choose a controller in the servomechanism class. The most common and probably the easiest to design is the proportional-plus-integral-plus-derivative (PID) compensator. For these reasons we examined this controller first and found that it performed very well in this application.

The PID compensator uses an error between two variables to generate a signal which is fed to the part of the system that is to be controlled, known as the *plant*. The input to the PID

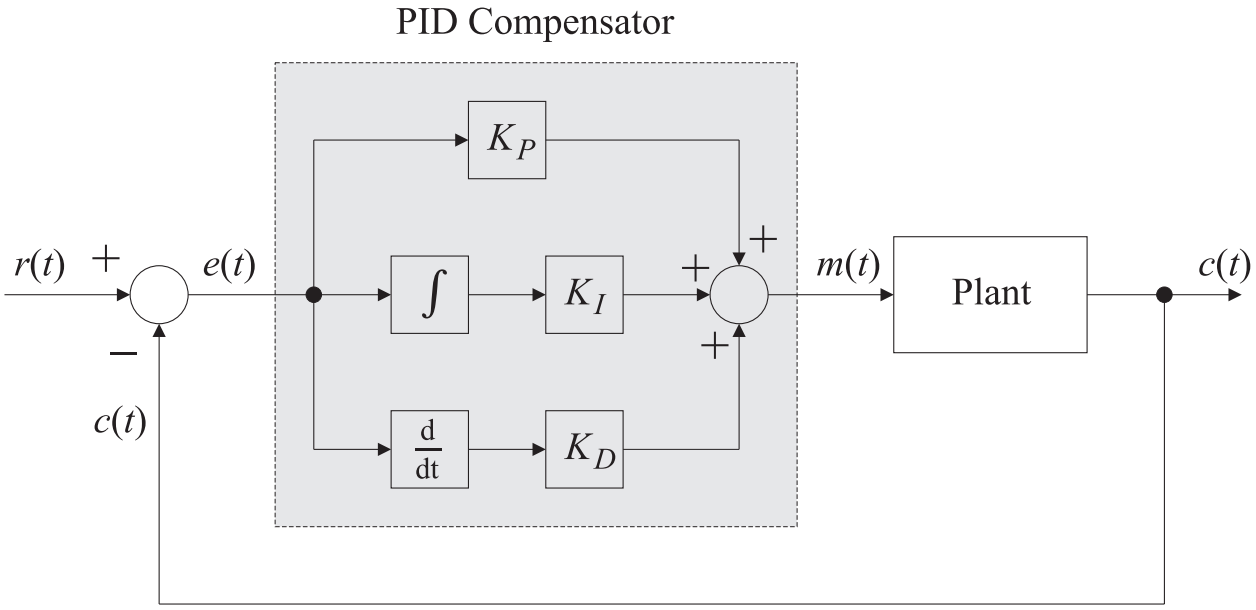

Figure 4.1: Block diagram of a system with a PID compensator.

compensator is an error signal $e(t)$, which is defined by

$$e(t) = r(t) - c(t) \tag{4.1}$$

where $r(t)$ is the reference signal and $c(t)$ is the actual value of the controlled variable. The output of the PID compensator $m(t)$ is a function of this error signal and is given by

$$m(t) = K_P e(t) + K_I \int e(t)dt + K_D \dot{e}(t) \tag{4.2}$$

where K_P, K_I, and K_D are constant gains. A block diagram of a PID compensated system is shown in Figure 4.1.

The PID compensator is a single input, single output (SISO) controller. Therefore, we must analyze each axis of the robot individually. A block diagram of one axis of the ship-motion simulation platform is shown in Figure 4.2. In this system the encoder on each motor is used to read the position of the motor shaft. Knowing the gear ratio in the gearbox, we can easily calculate the actual position of the input link of the four-bar linkage, which we will

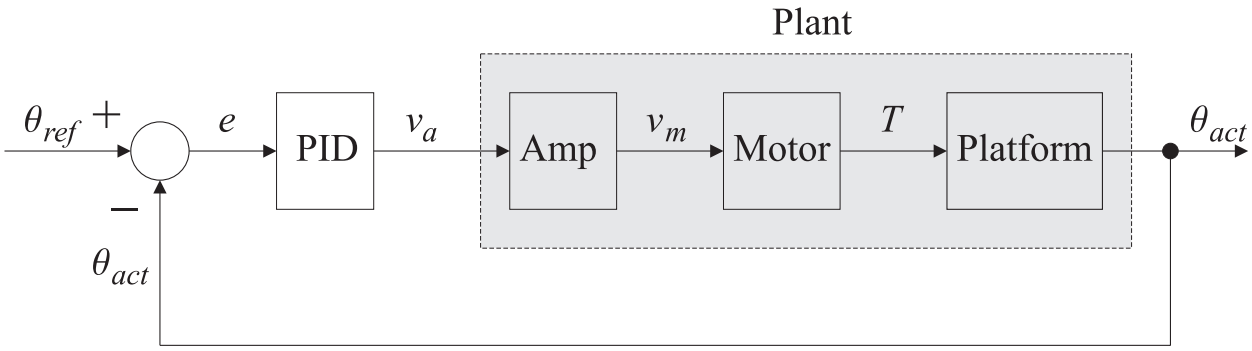

Figure 4.2: Block diagram of one axis of the ship-motion simulation platform.

denote as θ_{act}. The desired position of the input link θ_{ref} can be calculated using the inverse kinematics detailed in Chapter 3. The error between these two signals is calculated using Eq. (4.1) and the output of the PID controller is calculated using Eq. (4.2). In our case the output of the PID compensator is a voltage sent to the servo motor amplifier, which can be considered part of the plant. The motor and the platform constitute the remainder of the plant.

4.2 Root-Locus Analysis

The root locus is a plot of the location of the poles of a closed-loop transfer function in the s-plane as some system parameter is varied. Since the locations of the poles of a system reveal information about the behavior of the system, the root locus is a very useful design tool. Once a root locus has been generated, a designer can choose the location of any pole in the system and find the corresponding control parameter value and the positions of the other poles.

A block diagram of a general system with a control parameter is shown in Figure 4.3. The closed-loop transfer function $G_{CL}(s)$ of this system is

$$G_{CL}(s) = \frac{KG_C(s)G_P(s)}{1 + KG_C(s)G_P(s)} \tag{4.3}$$

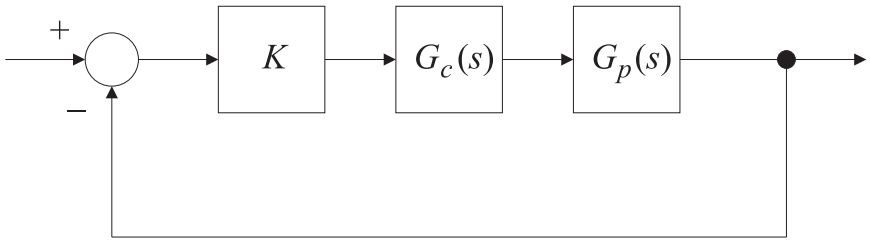

Figure 4.3: Block diagram of a general system with a control parameter.

where K is a real-valued control parameter with $0 < K < \infty$, $G_C(s)$ is the transfer function of the compensator, and $G_P(s)$ is the transfer function of the plant [19]. The root locus is generated by solving for the roots of the characteristic equation as the control parameter K is varied. The characteristic equation

$$1 + KG_C(s)G_P(s) = 0 \tag{4.4}$$

is found by setting the denominator of the closed-loop transfer function equal to zero.

We must choose the values of the three gains, K_P, K_I, and K_D, in the PID controller. If we first choose the ratios $\frac{K_P}{K_D}$ and $\frac{K_I}{K_D}$, we can design the PID compensator using the root-locus procedure. Each gain has a certain effect on the system: K_P affects the speed of the response, K_I affects the steady-state error in the system, and K_D affects the transient response of the system. We elected to set $K_I = 0$ because we found in our experiments that acceptable steady-state errors were achievable without this gain. This reduces our control algorithm to a PD compensator.

In order to use the root-locus procedure, we first need to develop a transfer function for our system. Since the platform has three motors, we will need three independent PD controllers, one for each motor. This requires the assumption that each motor can be modeled independently of the other two motors. In other words, when analyzing one motor, we assumed that the other two were not moving. In order to derive a transfer function for our system, we found a transfer function for each block in the block diagram shown in Figure 4.2 and then

combined them to find the overall system transfer function.

First, we will derive the transfer function of the PD compensator. The Laplace transform of Eq. (4.2) is

$$M(s) = K_P E(s) + K_I \frac{1}{s} E(s) + K_D s E(s) \tag{4.5}$$

Setting $K_I = 0$ and rearranging gives us the transfer function for a PD compensator:

$$G_C(s) = \frac{M(s)}{E(s)} = K_P + K_D s \tag{4.6}$$

It is useful to rewrite this equation as

$$G_C(s) = K_D(a + s) \tag{4.7}$$

where $a = \frac{K_P}{K_D}$. When one designs with the root-locus procedure, the ratio a between the gains can be chosen first. The controller introduces a zero in the root locus at $(-a, 0)$. After the value of a is chosen, K_D can be used as the control variable in the root-locus procedure.

Next, we consider the amplifier. Since the amplifier dynamics are much faster than the dynamics of the rest of the system, we will simply treat the amplifier block as a constant gain. We can write

$$v_m(t) = K_a v_a(t) \tag{4.8}$$

where $v_m(t)$ is the output voltage of the amplifier, K_a is the amplifier gain, and $v_a(t)$ is the input voltage to the amplifier. Taking the Laplace transform of Eq. (4.8) and rearranging yields the amplifier transfer function:

$$G_A(s) = \frac{V_m(s)}{V_a(s)} = K_a \tag{4.9}$$

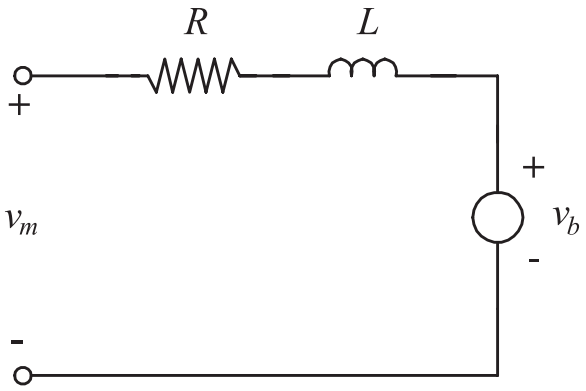

Figure 4.4: Motor armature circuit.

The platform can be modeled as an inertia attached to the motor shaft; therefore, we will model the motor and platform together. For a DC servo motor with a constant field flux, the motor torque T is proportional to the armature current i:

$$T(t) = K_m i(t) \tag{4.10}$$

where K_m is the motor torque constant [19]. Using Kirchhoff's Voltage Law to sum voltages around the armature circuit shown in Figure 4.4, we find that

$$v_m(t) = Ri(t) + L\frac{di(t)}{dt} + v_b(t) \tag{4.11}$$

where $v_m(t)$ is the voltage applied across the motor armature, R is the armature resistance, L is the armature inductance, and $v_b(t)$ is the back-*emf* voltage. The back-*emf* voltage is generated due to the rotational motion of the motor armature and is proportional to the angular velocity of the motor shaft. Thus,

$$v_b(t) = K_b\frac{d\theta(t)}{dt} \tag{4.12}$$

where K_b is the back-*emf* constant. Most servo motors have a very small inductance and accordingly this term is often set equal to zero in order to simplify the equations. Assuming that $L = 0$, substituting Eq. (4.12) into Eq. (4.11), and solving for the armature current, we

find

$$i(t) = \frac{1}{R}\left[v_m(t) - K_b\frac{d\theta(t)}{dt}\right] \tag{4.13}$$

Substituting this equation into Eq. (4.10) we obtain

$$T(t) = \frac{K_m}{R}\left[v_m(t) - K_b\frac{d\theta(t)}{dt}\right] \tag{4.14}$$

Assuming no friction or air resistance and summing the moments on the motor shaft yields

$$T(t) = I\frac{d^2\theta(t)}{dt} \tag{4.15}$$

where I is the mass moment of inertia of the motor shaft plus the inertia due to the platform. Substituting Eq. (4.15) into Eq. (4.14) gives us

$$I\frac{d^2\theta(t)}{dt} = \frac{K_m}{R}\left[v_m(t) - K_b\frac{d\theta(t)}{dt}\right] \tag{4.16}$$

Taking the Laplace transform of this equation yields

$$Is^2\Theta(s) = \frac{K_m}{R}\left[V_m(s) - K_b s\Theta(s)\right] \tag{4.17}$$

Rearranging Eq. (4.17) yields the transfer function of the motor and platform $G_{MP}(s)$:

$$G_{MP}(s) = \frac{\Theta(s)}{V_a(s)} = \frac{K_m}{RIs^2 + K_mK_bs} \tag{4.18}$$

The transfer function of the plant $G_P(s)$ is

$$G_P(s) = G_A(s)G_{MP}(s) = \frac{K_aK_m}{RIs^2 + K_mK_bs} \tag{4.19}$$

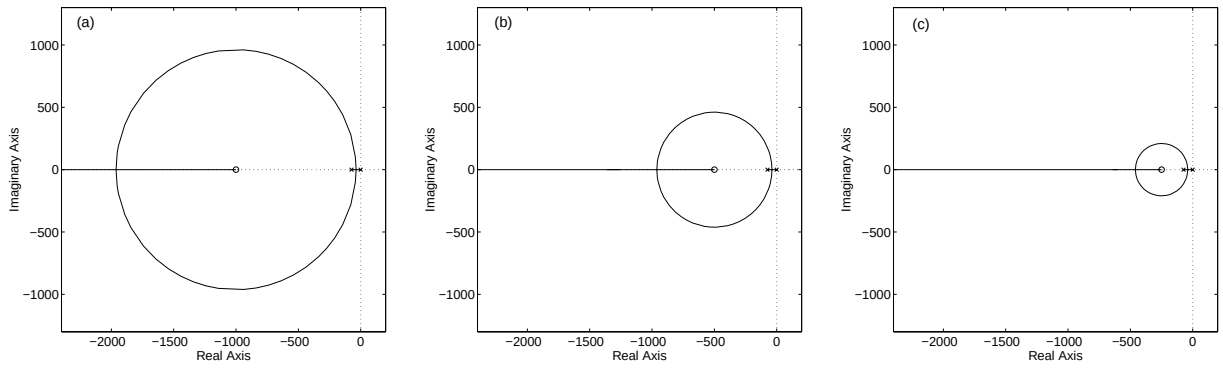

Figure 4.5: Root loci for (a) $a = 1000$, (b) $a = 500$, and (c) $a = 250$.

Using Eq. (4.3) and setting $K = 1$ we find the closed-loop transfer function $G_{CL}(s)$:

$$G_{CL}(s) = \frac{G_C(s)G_P(s)}{1 + G_C(s)G_P(s)} = \frac{K_D K_a K_m (a + s)}{RIs^2 + K_m K_b s + K_D K_a K_m (a + s)} \tag{4.20}$$

The values of the constants for the Baldor motors that we used are $R = 1.2\ \Omega$, $K_m = 0.381$ N·m/A, $K_b = 0.381$ N·m/A, and $L = 4.6$ mH. The amplifier gain was set equal to $K_a = 9$. The moment of inertia used for our model was $I = 16.43 \times 10^{-4}$ kg·m^2. This represents the inertia of the motor shaft plus the inertia of the gearbox. The inertia of the gearbox was considered sufficient to represent the entire platform for the purpose of designing the PD controller.

Root loci were drawn for several values of a and are shown in Figure 4.5. As a is increased note the change in the location of the zero, indicated by the circle ($\circ$). The open-loop poles are indicated by x's. The location of the closed-loop poles on the locus is determined by the value of the control parameter K_D. Gains were calculated for several combinations of a and K_D. We tried to choose a value of K_D which would locate the closed-loop poles at angles of $\pm 45^\circ$ from the negative real axis. This location corresponds to a damping ratio of 0.707. The smoothest operation of the platform was found using $a = 800$ and $K_D = 0.00244$. A root locus for $a = 800$ is shown in Figure 4.6. The closed-loop poles are located at the open-loop poles for $K = 0$. The arrows indicate the direction of travel of the poles along

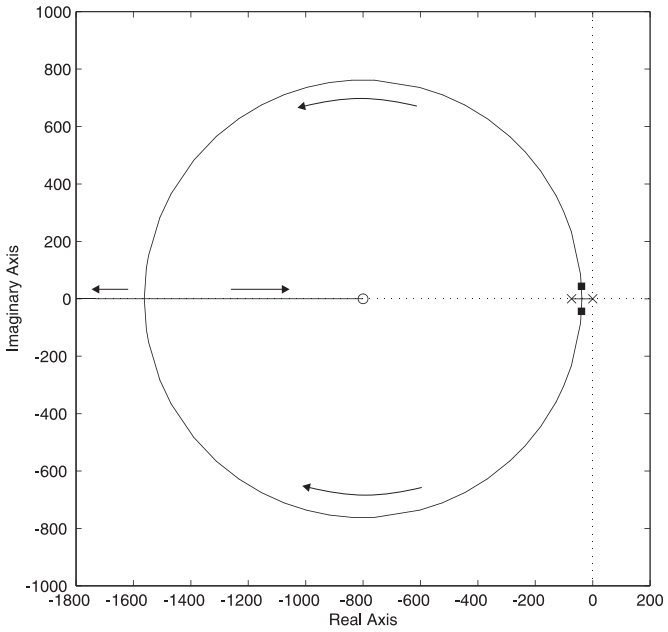

Figure 4.6: Root locus with $a = 800$.

the root locus as K_D is increased. At $K = \infty$, one pole goes to the zero and the other goes to negative infinity on the real axis. The location of the poles corresponding to a value of $K_D = 0.00244$ are marked by the squares (■). We notice that these poles are located approximately $\pm 45^\circ$ from the negative real axis. With $K_D = 0.00244$ and $a = 800$, we find that $K_P = 1.95$. Figure 4.7 shows the step response of the closed-loop model with $K_P = 1.95$ and $K_D = 0.00244$.

4.3 Hardware

A commercial servo control board installed in a desktop computer was used to execute the control algorithm. The control board is capable of controlling up to four axes of motion simultaneously. This includes the ability to read four encoders and output four 16-bit resolution analog control signals to the amplifiers. The board also accepts limit and home switch signals and has eight general purpose digital inputs and outputs. The general purpose digital

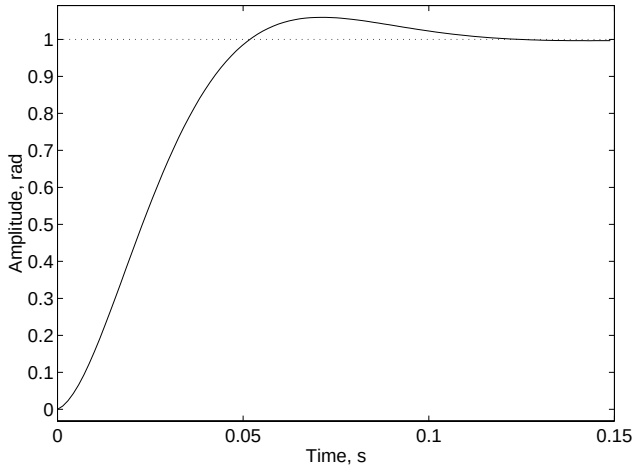

Figure 4.7: Step response of the closed-loop system with $K_D = 0.00244$ and $K_P = 1.95$.

inputs and outputs are used to control the motor brakes and read amplifier fault signals. The computer used is a Pentium II 266 MHz machine with 64 MB of RAM.

4.4 Software

The kinematics developed in the previous chapter and the control algorithm developed in this chapter were programmed in C as a DOS application. A flowchart of the main portion of the code is shown in Figure 4.8. The user is first given an opportunity to change the motion parameters from the default values. These parameters include amplitudes, frequencies, and the runtime. Next the program uses the kinematics developed in Chapter 3 to calculate the desired motor positions and velocities at each time step and saves these values in data files. The software calculates and stores these values before the main loop is entered in order to enable smaller time steps, which improves the quality of the motion. When these calculations have been completed, the software begins a homing routine which calibrates the position of the platform. In this routine each motor drives its associated basal leg upward until it reaches the upper limit switch. The encoder counts are then zeroed and the motors lower each leg

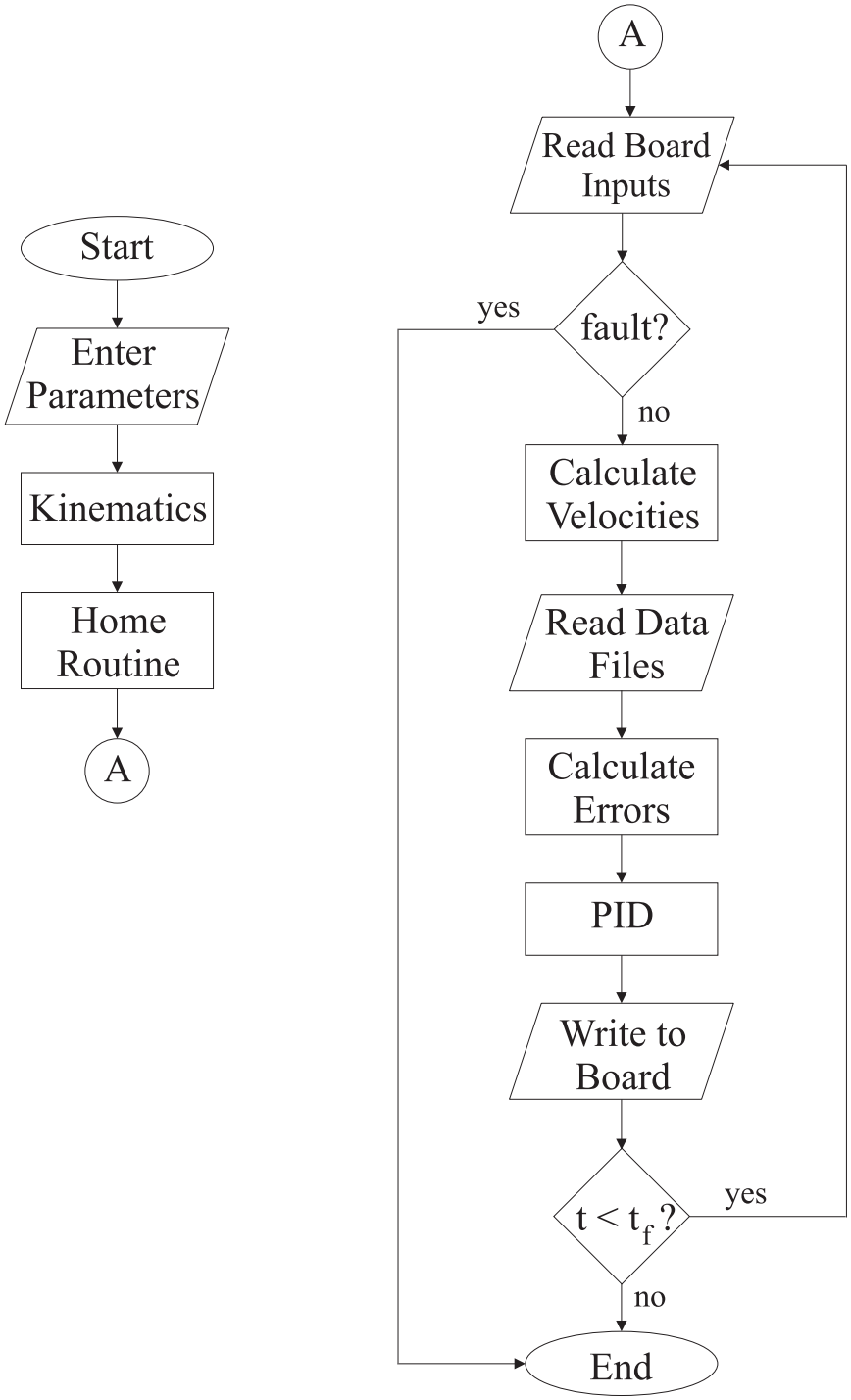

Figure 4.8: Flowchart for the control software.

an equal distance placing the platform at a position near the center of the workspace. The encoder counts are zeroed again at this position. Now the ship-motion simulation loop is entered. At each time step the code reads information from the control board including the encoder positions, the states of the limit switch inputs, and the states of the general purpose inputs. The code checks for faults such as an amplifier fault or a limit switch that has been triggered. If one or more faults are detected the program is terminated immediately. If no faults have occurred, the actual motor velocities are calculated numerically using position data saved from the past several time steps. Next, the desired motor positions and velocities are read from the data files and the position and velocity errors are calculated and used as inputs to the PD controllers. The output from the PD controllers is written to registers on the control board. The board automatically converts the digital values to analog voltages which are sent to the motor amplifiers. Finally, the code compares the current time to the total requested runtime. If the current time is less than the total runtime the loop is continued. If the current time is equal to or greater than the total runtime the loop is exited, the voltages to the motors are zeroed, and the brakes are engaged.

4.5 Performance

To evaluate the performance of the software and the PD controller, we tested the platform with several motion profiles. Figure 4.9 shows the actual input link angles compared to the desired angles calculated with the kinematics during one of these test runs. In this test, the platform was programmed to reproduce sinusoidal motions with amplitudes of 2° in roll, 1° in pitch, and 0.5 inches in heave. The pitch and roll frequencies were 0.5 Hz and the heave frequency was 1 Hz. The simulated center of gravity of the ship was located approximately at the midjoint of leg pair one. The crane was not mounted on the platform during this test. We see that the actual motion of the legs was qualitatively similar to the desired motion. Slight overshoots and undershoots are visible as well as a small lag of the actual positions

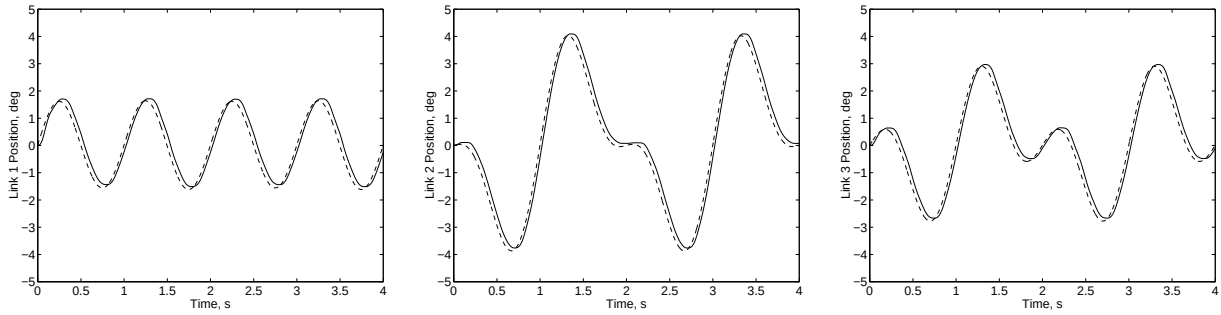

Figure 4.9: Actual link angles compared to desired link angles in a test run. The dashed lines represent the reference values and the solid lines represent the actual motion of the links.

behind the desired positions.

Chapter 5

2-D Crane Control Strategy

Load pendulations in the plane of the boom can be reduced by simply controlling the boom luff angle. The boom luff angle specifies the location of the boom as it pivots up and down. This degree of freedom already exists in ship-mounted cranes, and therefore modifying the hardware of current cranes would be limited to the addition of a few sensors and the electronics needed to execute the control algorithm. The control strategy developed in this chapter is based on time-delayed position feedback of the load-cable angle. This control algorithm can be superimposed transparently on the input of the crane operator. The control and stability of systems with inherent time delays have been investigated extensively in the past (e.g., [1, 14, 17, 20, 23–25]); however, the use of time-delayed position feedback to control systems with no inherent time delay is relatively new. Recently, Olgac and Holm-Hansen used the concept of time-delayed position feedback control to tune a spring-mass-damper vibration absorber [16].

5.1 Mathematical Model

The model used to develop the controller is a planar pendulum with a rigid massless cable and a massive point load, as shown in Figure 5.1. The boom tip is represented by point P and the load, with mass m, is at point G. The boom tip is located with respect to an inertially fixed coordinate frame by the vector $\mathbf{r_P} = (x_p, y_p)$. The position $\mathbf{r_G}$ of G is given by

$$\mathbf{r_G} = \mathbf{r_P} + l(\sin\theta\mathbf{i} - \cos\theta\mathbf{j}) = (x_p + l\sin\theta)\mathbf{i} + (y_p - l\cos\theta)\mathbf{j} \tag{5.1}$$

Then the equation of motion of the pendulating cargo, which includes a term that accounts for air resistance on the cable and cargo, is given by

$$\Sigma\mathbf{Forces} = T(-\sin\theta\mathbf{i} + \cos\theta\mathbf{j}) - mg\mathbf{j} - C_D(\dot{x}_p\cos\theta + \dot{y}_p\sin\theta + l\dot{\theta})(\cos\theta\mathbf{i} + \sin\theta\mathbf{j}) = m\ddot{\mathbf{r}}_\mathbf{G} \tag{5.2}$$

where T is the tension in the cable, C_D is the drag coefficient (here we assume that the drag is linearly related to the velocity), and $\mathbf{i}$ and $\mathbf{j}$ are the familiar Cartesian base vectors. Equation (5.2) can be manipulated to yield the following equation for θ:

$$\ddot{\theta}(t) + 2\mu[\dot{\theta}(t) + \dot{\xi}(t)\cos\theta(t) + \dot{\eta}(t)\sin\theta(t)] + \frac{g}{l}\sin\theta(t) + \ddot{\xi}(t)\cos\theta(t) + \ddot{\eta}(t)\sin\theta(t) = 0 \tag{5.3}$$

where $2\mu = \frac{C_D}{m}$, $\xi(t) = \frac{x_p(t)}{l}$, and $\eta(t) = \frac{y_p(t)}{l}$.

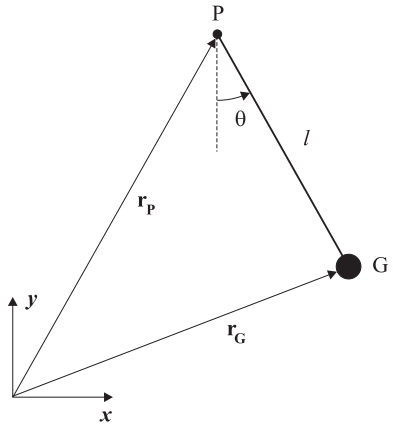

Figure 5.1: Schematic diagram of model

5.2 Controller Design

The controller is based on time-delayed feedback of the angle θ. This time-delayed feedback creates a damping effect in the system. The control law is

$$x_p(t) = x_0(t) + kl\sin[\theta(t-\tau)] \tag{5.4}$$

where x_0 is some reference position, k is a gain, and τ is the time delay applied to the feedback of the load angle. Throughout this thesis $x_0(t)$ is treated as a constant; however this could be a time-varying term, such as the position commanded by the crane operator or the position of the desired landing point on the smaller craft.

For the purpose of designing the controller, we assume that there is no motion of the boom tip in the y direction and that the only excitation in the x direction is that of the controller. Substituting Eq. (5.4) into Eq. (5.3) and setting $\dot{y}_p(t) = \ddot{y}_p(t) = 0$, we obtain the following equation of motion of the controlled system:

$$\ddot{\theta}(t) + 2\mu\{\dot{\theta}(t) + k\dot{\theta}(t-\tau)\cos[\theta(t-\tau)]\cos\theta(t)\} + \frac{g}{l}\sin\theta(t) + k\{\cos[\theta(t-\tau)]\ddot{\theta}(t-\tau) - \sin[\theta(t-\tau)](\dot{\theta}(t-\tau))^2\}\cos\theta(t) = 0 \tag{5.5}$$

5.3 Linear Analysis

To insure a good choice of τ and k, we linearize the system and study the linear stability. Linearizing Eq. (5.5) yields

$$\ddot{\theta}(t) + 2\mu\dot{\theta}(t) + 2\mu k\dot{\theta}(t-\tau) + \frac{g}{l}\theta(t) + k\ddot{\theta}(t-\tau) = 0 \tag{5.6}$$

The solution of Eq. (5.6) can be expressed as

$$\theta(t) = ae^{\sigma t}\cos(\omega t + \theta_0) \tag{5.7}$$

where a, σ, ω, and θ_0 are real constants. Substituting Eq. (5.7) into Eq. (5.6) and setting the coefficients of both $\cos(\omega t + \theta_0)$ and $\sin(\omega t + \theta_0)$ equal to zero, we obtain

$$2k\omega(\mu+\sigma)\sin\omega\tau + k(\sigma^2 + 2\mu\sigma - \omega^2)\cos\omega\tau + (\sigma^2 + \frac{g}{l} - \omega^2 + 2\mu\sigma)e^{\sigma\tau} = 0 \tag{5.8}$$

$$k(\sigma^2 + 2\mu\sigma - \omega^2)\sin\omega\tau - 2k\omega(\mu+\sigma)\cos\omega\tau - 2\omega(\mu+\sigma)e^{\sigma\tau} = 0 \tag{5.9}$$

which for a given k and τ can be solved for ω and σ; a and θ_0 are determined from the initial conditions. The system is stable or unstable depending on whether σ is negative or positive. The transition conditions separating stability from instability correspond to $\sigma = 0$. To determine these conditions, we substitute $\sigma = 0$ into the equations above and obtain

$$\frac{g}{l} - \omega^2(1 + k\cos\omega\tau) + 2k\mu\omega\sin\omega\tau = 0 \tag{5.10}$$

$$2\mu + 2k\mu\cos\omega\tau + k\omega\sin\omega\tau = 0 \tag{5.11}$$

We vary τ, solve Eqs. (5.10) and (5.11) for ω and k, and find the linear stability boundaries, which are shown in Figure 5.2. The shaded regions correspond to unstable motions and the unshaded regions correspond to stable motions. The parameters used to generate this plot

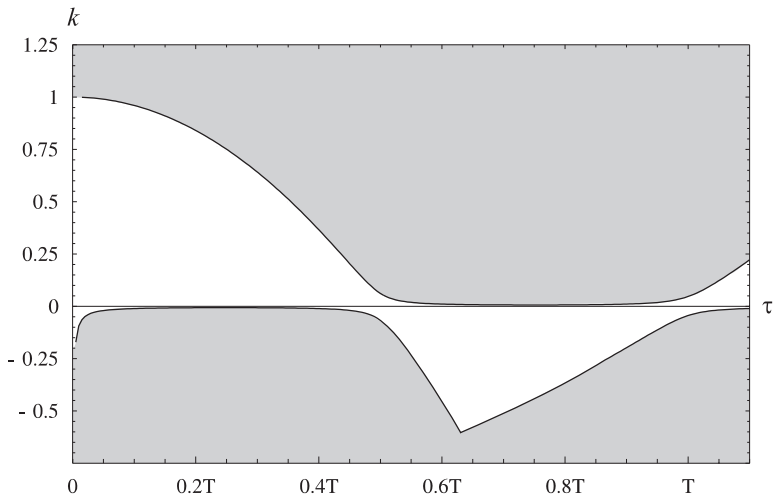

Figure 5.2: Linear stability diagram, where k is the feedback gain and τ is the time delay in terms of the period T of the uncontrolled linear system. The shaded areas are unstable regions.

were taken from the 1/24th scale model crane. Here, $l = 3.33$ ft, $g = 32.2$ ft/sec^2, and μ was experimentally determined to be 0.01 sec^{-1}.

By varying τ and k in Eq. (5.8) and Eq. (5.9) and solving for ω and σ, we can find the amount of damping for a given τ and k. A contour plot of the damping versus τ and k, again generated using the parameters above, is shown in Figure 5.3. Here darker shading corresponds to regions of higher damping. When choosing parameter values, the designer should first select a value for k based upon the allowable amount of boom motion. Larger values of k will allow larger boom displacements. Once k has been chosen, τ should be set to the value where the greatest damping can be found in Figure 5.3 for the selected value of k.

5.4 Kinematics

When the control is implemented on the crane, we actually control the boom angle, not the x position of the boom tip directly. This requires the development of a kinematic relation

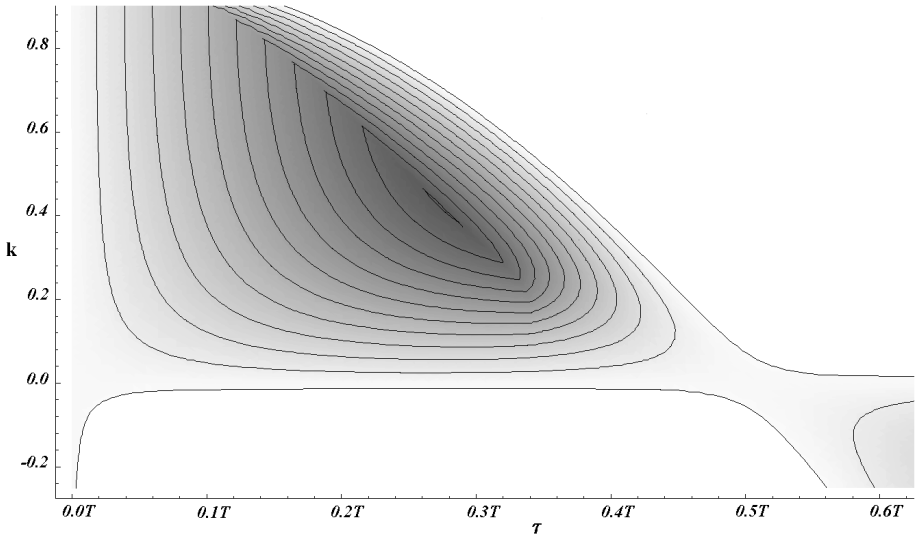

Figure 5.3: Contour plot of the damping as a function of k and τ, where τ is given in terms of the period T of the uncontrolled system. Darker areas correspond to regions of higher damping.

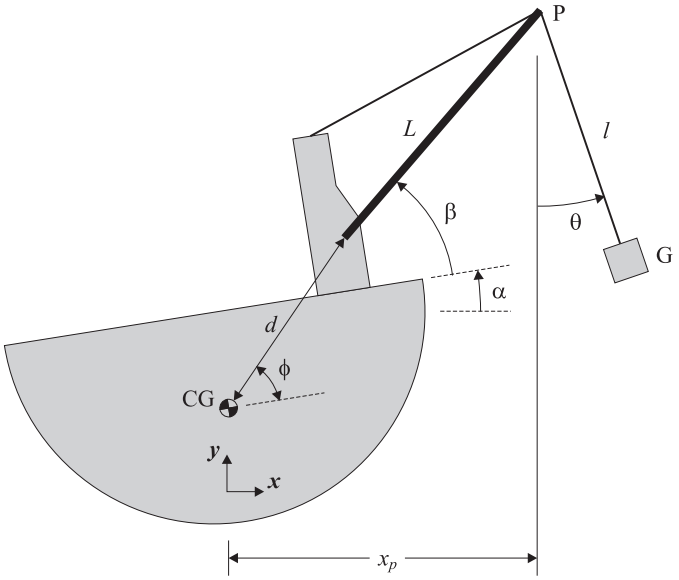

Figure 5.4: Schematic diagram of the ship and crane.

between the x position of the boom tip and the boom angle.

Figure 5.4 shows a schematic diagram of the ship and crane when the boom is oriented perpendicular to the axis of the ship. Here, d and ϕ are constants determined by the ship's geometry, L is the boom length, α is the roll angle of the ship, and β is the angle of the boom relative to the ship's deck. If the ship's center of gravity CG lies along the same vertical line as the origin of the inertial coordinate system in Figure 5.1, then

$$x_p(t) = d\cos[\phi + \alpha(t)] + L\cos[\beta(t) + \alpha(t)] \tag{5.12}$$

Solving for the boom angle β, we find

$$\beta(t) = \cos^{-1}\left(\frac{x_p(t) - d\cos[\phi + \alpha(t)]}{L}\right) - \alpha(t) \tag{5.13}$$

Finally, substituting Eq. (5.4) into Eq. (5.13), we obtain

$$\beta(t) = \cos^{-1}\left(\frac{x_0(t) + kl\sin[\theta(t-\tau)] - d\cos[\phi + \alpha(t)]}{L}\right) - \alpha(t) \tag{5.14}$$

5.5 Implementation

Now that the desired boom angle has been found we must determine the necessary amount of torque to apply to the boom in order to achieve the proper boom angle. There are two ways to do this.

The first is to determine the proper amount of torque directly from the dynamics of the crane. A block diagram of this approach is shown in Figure 5.5a. We begin by summing the moments on the boom to obtain

$$T_b = I_b(\ddot{\beta} + \ddot{\alpha}) - \Sigma M \tag{5.15}$$

where T_b is the control torque applied to the boom, I_b is the mass moment of inertia of the boom about its center of gravity, $\ddot{\beta}$ is the angular acceleration of the boom relative to the deck of the ship, $\ddot{\alpha}$ is the angular acceleration of the ship in roll, and ΣM is the sum of all moments about the center of gravity of the boom other than the control torque.

If we know all of the quantities on the right hand side of Eq. (5.15), we can use the equation to calculate the torque on the boom necessary to keep the boom at the angle β given in Eq. (5.14). The mass moment of inertia of the boom about its center of gravity I_b can be calculated given the geometry and mass distribution of the boom. We can differentiate Eq. (5.14) twice to determine the desired angular acceleration of the boom relative to the ship's deck $\ddot{\beta}$ as a function of time. The angular acceleration of the ship in roll $\ddot{\alpha}$ can be measured with a sensor. The moments on the boom other than the control torque include the moment due to the tension in the load hoist cable, the moment due to any force at the boom pivot point, and moments due to any other forces on the boom, such as friction or the wind. The moments due to the tension in the load hoist cable and the force at the boom pivot point could be calculated from measured quantities. The other moments could probably be ignored without introducing significant error.

The motor used to actuate the boom is normally not connected directly to the boom. To generate a mechanical advantage, a cable attached to the motor shaft is passed around several pulleys before connecting to the boom. Therefore, after calculating the torque required on the boom T_b, it is necessary to use some kinematics to calculate the corresponding torque at the motor shaft T_m. The motor shaft torque should be divided by some torque constant to obtain the value of the control signal that is sent to the amplifier. The value of this torque constant depends on the amplifier and motor used.

Ideally we could measure all of the quantities necessary to calculate the terms in Eq (5.15) with sensors mounted at various places on the ship and crane. Unfortunately, the sensors used in our experiments did not provide enough resolution to determine precisely the angular accelerations that appear after differentiating Eq. (5.14) twice. Therefore, we were unable to calculate the angular acceleration of the boom relative to the ship to a reasonable precision. This forced us to develop another method for determining the amount of torque to apply to the boom.

Instead of calculating the torque directly using the dynamics of the crane, we can simply treat the boom angle calculated in Eq. (5.14) as a reference signal and use a PID compensator to position the boom. While we may use a dynamic model of the boom to help us determine appropriate gains for this secondary controller, the knowledge of the exact boom dynamics becomes less critical with this method. To use a PID controller, we measure the actual boom angle, calculate the error between it and the desired boom angle, and feed this error to the PID compensator. As with the first approach, kinematics will be needed to calculate the motor torque from the torque output by the PID compensator. This motor torque should again be divided by a torque constant to generate the control signal that is sent to the amplifier. A block diagram of this method is shown in Figure 5.5b. The PID compensator can be designed using an approach similar to the one used in Chapter 4 with the platform motors. For this reason, we do not present the details of the development of the secondary controller. We used this second method of implementing the control in both our numerical simulations

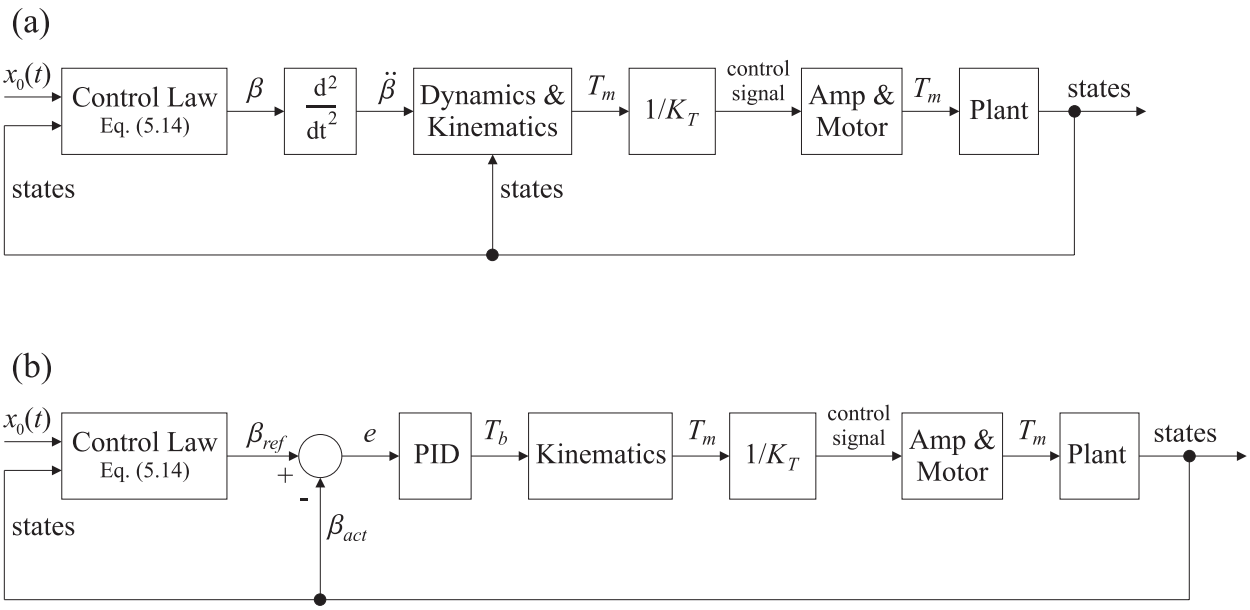

Figure 5.5: Block diagrams showing alternate methods of implementing the control.

and our experiments since it requires less accurate knowledge of the boom dynamics and the calculations do not depend on any angular accelerations.

Chapter 6

Results

6.1 Numerical Simulation

We constructed a 2D computer model based on the dimensions of the T-ACS 1 crane and ship, which are given in Table 6.1. The dimensions of the other T-ACS ships may vary slightly from these dimensions. Figure 6.1 shows a scale drawing of the geometry of the computer model. The center of gravity of the load was located 89 ft below the boom tip making the natural frequency of the cargo pendulation 0.096 Hz. Our model used the location of Crane 2. The crane was oriented so that the boom extended over the side of the ship and was perpendicular to the axis of the ship. The boom was modeled as a rigid beam with a uniform mass distribution along its length and the ship was excited sinusoidally in roll and heave. There was no damping in this model.

The boom was actuated using a control torque applied directly to the boom. We used the control algorithm outlined in Section 5.5 and shown in Figure 5.5b with some modifications. Since the torque output from the PID compensator was applied directly to the boom, the kinematics block, the torque constant block, and the amplifier and motor block were not

Table 6.1: Dimensions of the T-ACS 1 ship and crane.

		Distance, ft
Ship Dimension	LBP	633
	Beam	76
	KG	21.81
	GM	9.42
Crane 1 Location	Fwd of Midships	192
	Stbd of Centerline	25
	Waterline at Bottom of Slew Ring	69 above keel
Crane 2 Location	Fwd of Midships	59.5
	Stbd of Centerline	27.17
	Waterline at Bottom of Slew Ring	69.83 above keel
Crane 3 Location	Aft of Midships	233
	Stbd of Centerline	27.17
	Waterline at Bottom of Slew Ring	71.00 above keel
Crane Dimension	Boom Length	121

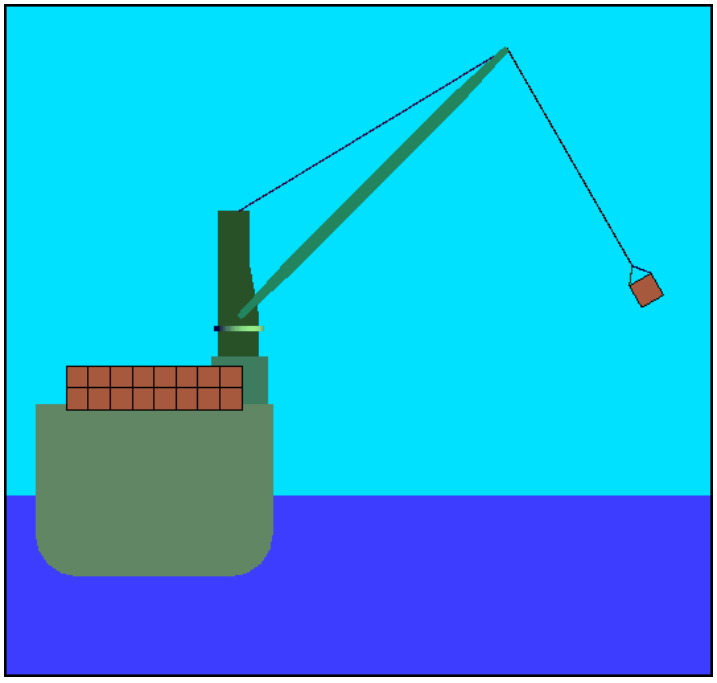

Figure 6.1: Scale drawing of the geometry used in the computer model.

needed. Results were obtained by numerically integrating the full nonlinear equations of motion.

6.2 Experimental Validation

Experimental validation was conducted with a 1/24.175 scale model of a T-ACS 1 crane mounted on the platform described in Chapter 2. Although the platform is capable of producing arbitrary heave, pitch, and roll motions, the excitations in these experiments were sinusoidal. The crane was again oriented so that the boom extended over the side of the ship and the platform was excited in roll and heave only. A picture of the scale model of the crane and the ship-motion simulation platform is shown in Figure 6.2.

The platform and scale model of the crane were instrumented with several sensors. A two-axis digital tilt sensor was mounted on the platform to read the pitch and roll angles of the ship, and an optical encoder was mounted at the boom pivot point to measure the angular displacement of the boom relative to the base of the crane. Two optical encoders were mounted at the boom tip to measure the angular displacement of the load cable relative to the boom. These encoders were mounted orthogonal to one another so that one measured the displacement in the plane of the boom and the other measured the out-of- plane displacement of the load cable. A brushless DC servo motor and amplifier were used to actuate the boom luff angle. A cable attached to the boom tip passed around several pulleys for mechanical advantage and then attached to a pulley on the motor shaft. A desktop computer sampled the sensor readings, calculated the required motor torque using the control law, and output the corresponding voltage to the amplifier.

The weight of the cargo was 3.0 lbs, which was scaled from a full size cargo weight of 44,800 lbs. The full size cargo container measures 8 ft high by 8 ft wide by 20 feet long. This results in model cargo dimensions of 4.0 inches high by 4.0 inches wide by 9.9 inches long. The

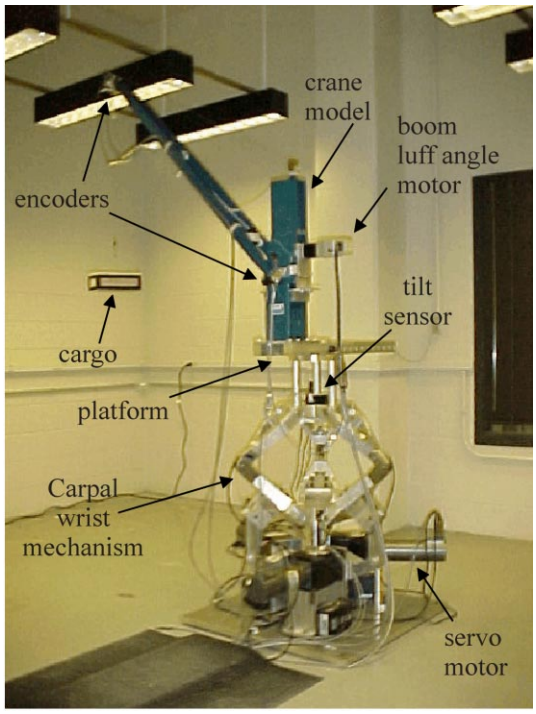

Figure 6.2: 1/24th scale model of T-ACS crane mounted on the three-degree-of-freedom ship-motion simulation platform.

distance between the boom tip and the center of gravity of the load was 3.33 ft making the natural frequency of the pendulum 0.495 Hz.

6.3 Effect of Frequency of Excitation

The mathematical model of the crane developed in Section 5.1 allows two types of excitation. This is apparent when we examine Eq. (5.3) and notice the terms involving $\ddot{x}_p(t)$ and $\ddot{y}_p(t)$. These terms represent the horizontal acceleration and the vertical acceleration of the boom tip, respectively. The frequencies of these excitations have a strong effect on the amplitude of the response. There are two critical resonances in our system. The first, known as primary resonance, occurs when the frequency of the horizontal excitation is equal to the linear natural frequency of the pendulum. The second, called the principal parametric resonance,

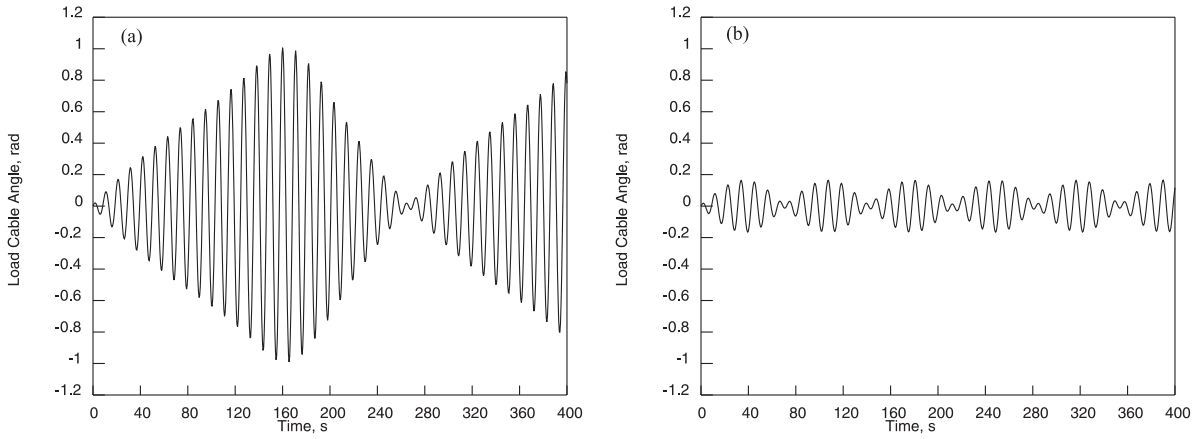

Figure 6.3: Uncontrolled responses in the numerical simulations for (a) excitation frequencies at the resonant frequencies and (b) excitation frequencies away from the resonant frequencies.

occurs when the frequency of the vertical excitation is equal to twice the linear natural frequency of the system. The effects of these resonances were demonstrated with numerical simulations and experiments.

The uncontrolled system was subjected to a harmonic excitation in roll at the linear natural frequency and a harmonic excitation in heave at twice the linear natural frequency in order to excite both the primary and principal parametric resonances. The response calculated numerically for a roll amplitude of 1° and a heave amplitude of 1 ft is shown in Figure 6.3a. Then the frequencies were detuned from the critical resonant frequencies by 15% while the amplitudes were kept at the same values. Figure 6.3b shows the numerically calculated response at these frequencies. Although the frequencies were only detuned from the resonant frequencies by 15%, the peak amplitude of the response was reduced by approximately 80%.

Similar results were obtained experimentally. Figure 6.4a shows the experimental response for excitations at the resonant frequencies, a roll amplitude of 1° and a heave amplitude of 0.5 inches. Unfortunately the experiment had to be stopped after 15 seconds because the amplitude had grown so large that the cargo was about to hit the boom. Figure 6.4b shows the experimental response for the same amplitudes as in (a), but with the frequencies detuned by 15% from the resonant frequencies.

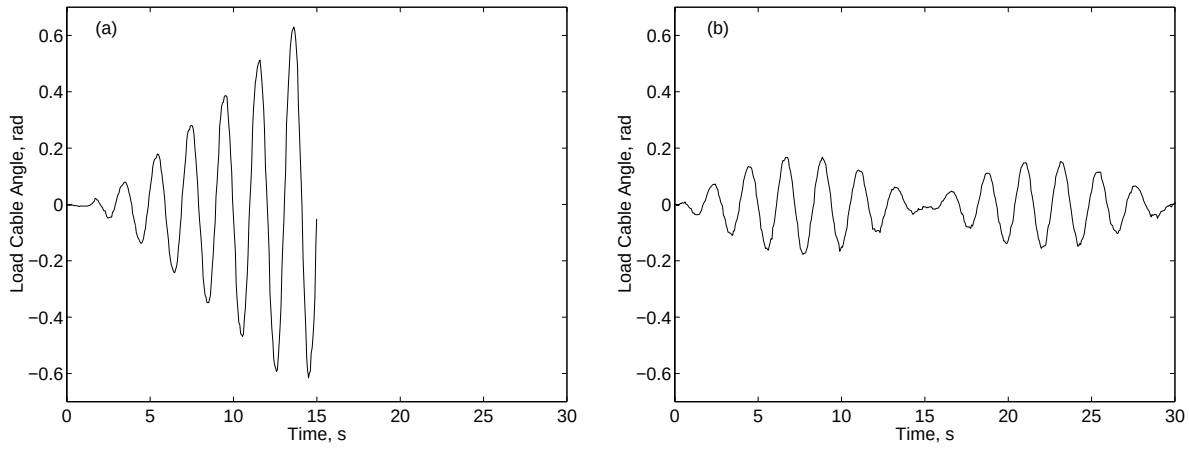

Figure 6.4: Uncontrolled experimental responses for (a) excitation frequencies at the resonant frequencies and (b) excitation frequencies away from the resonant frequencies.

6.4 Controlled Response

The controller provided a significant reduction in the amplitude of the response in both the numerical simulations and experiments. The crane was excited at the critical frequencies described above to test the controller's ability to suppress pendulations in a worst case scenario of ship motion.

Figure 6.5a shows the results of the numerical simulation for the controlled case compared to the uncontrolled case. The uncontrolled response is represented by the dashed line and the controlled response is represented by the solid line. The roll amplitude was 1° at a frequency of 0.096 Hz and the heave amplitude was 1 ft at a frequency of 0.19 Hz. In the controlled case, k was 0.05 and τ was 2.5 sec. A peak response amplitude reduction of 98.8% was achieved with the controller. Figure 6.5b shows the boom angle relative to the ship in the controlled case. The peak to peak displacement of the boom was only 0.06 rad or 3.4°.

Figure 6.6 shows the experimental results of the controlled and uncontrolled cases for excitation at the resonant frequencies. The roll amplitude was 1° at a frequency of 0.5 Hz and the heave amplitude was 0.5 inches at a frequency of 1.0 Hz. As shown in Figure 6.6a, these

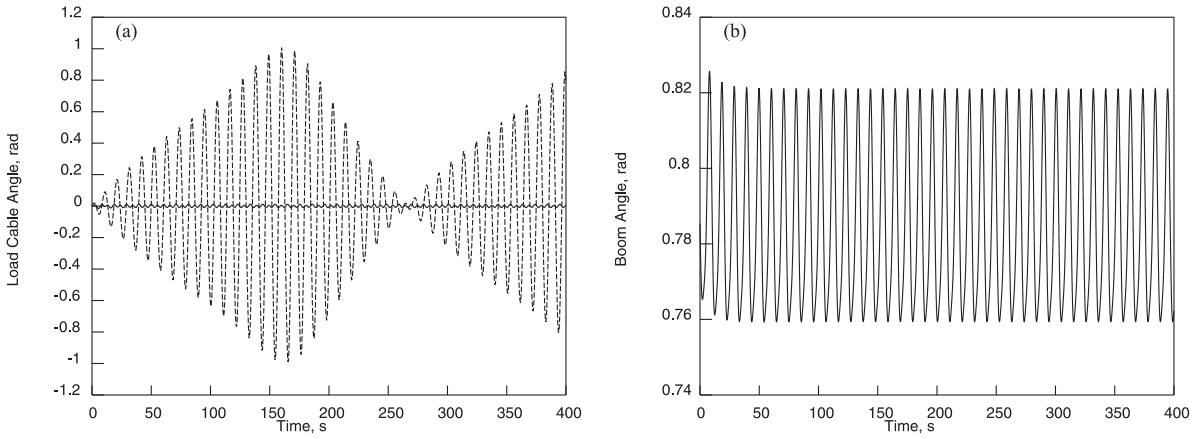

Figure 6.5: (a) shows the comparison of the controlled (solid line) and uncontrolled (dashed line) numerically calculated responses and (b) shows the boom angle relative to the ship in the controlled case.

excitation frequencies cause the amplitude of pendulation of the load to grow so rapidly in the uncontrolled case that the experiment had to be stopped after 15 seconds. In the controlled case, with $k = 0.5$ and $\tau = 0.55$ sec, the amplitude of pendulation remains bounded at approximately 0.10 rad or 5.7°. Figure 6.6b shows the boom angle relative to the ship in the controlled case. The boom had a maximum peak to peak displacement of about 0.14 rad or 8.0°.

6.5 Robustness

The controller is stable for large initial disturbances. The controlled system was subjected to the same forcing as in Section 6.4 and also given a large initial disturbance. Figure 6.7a shows the response calculated in the numerical simulation and Figure 6.7b shows the experimental response. In both cases the controller quickly damps the large pendulations and the response settles to a small steady-state oscillation. This occurs within 5 or 6 periods of oscillation for both the numerical and experimental responses.

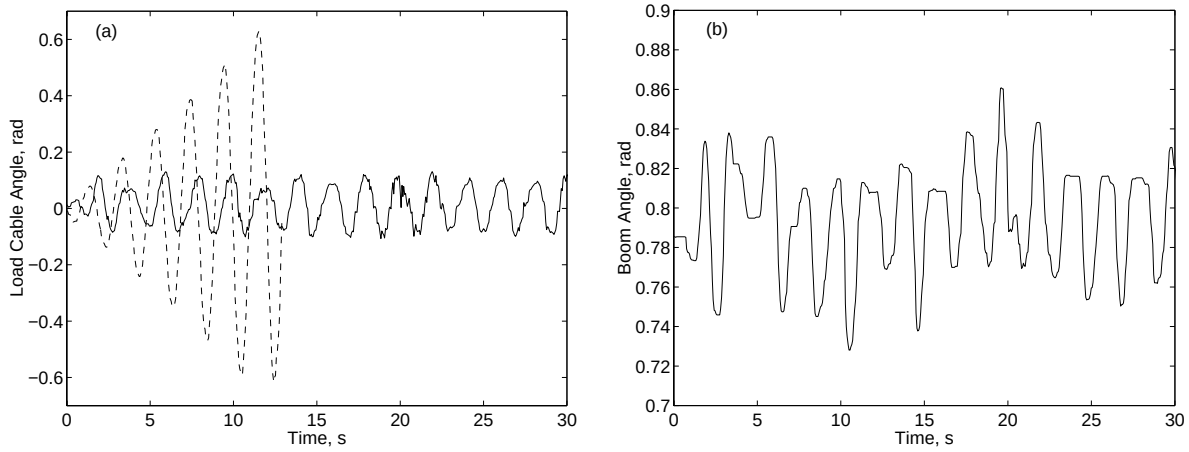

Figure 6.6: (a) shows the comparison of the controlled (solid line) and uncontrolled (dashed line) experimental responses and (b) shows the boom angle relative to the ship in the controlled case.

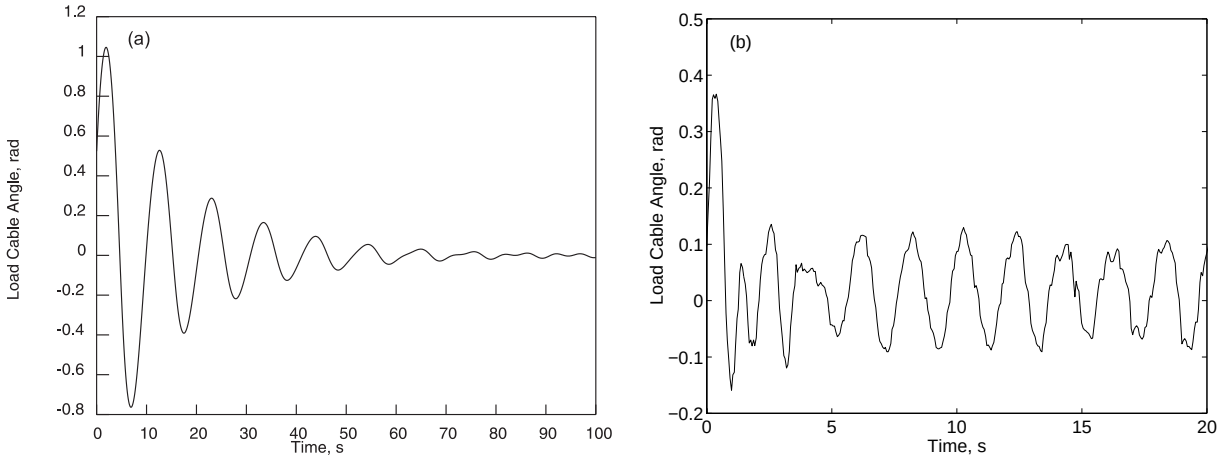

Figure 6.7: Initial condition response of the controlled system subject to forcing at the resonant frequencies: (a) shows the numerically calculated response and (b) shows the experimental response.

Chapter 7

Conclusions & Recommendations for Further Work

Boom-luff-angle actuation is an effective method for reducing cargo pendulations in the plane of the boom on ship-mounted cranes. A control law incorporating time-delayed position feedback of the load hoist cable angle was developed. Regions of stability in the parameter space were determined and a contour plot showing where the best damping values can be found was constructed. The effectiveness of the controller was demonstrated through numerical simulations and experiments.

As demonstrated in both the numerical simulations and the experiments, the frequency of excitation is critical. This means that the frequency of the waves in the seaway, not only their amplitude, is a critical factor in determining when dangerous conditions exist for crane operation.

Computer simulations showed a significant reduction in the amplitude of the in-plane pendulation for the controlled case over the uncontrolled case. The controller was also shown to be stable for large initial disturbances in the computer simulations. Experiments using a

scale model of a crane mounted on a moving platform validated the numerical results. The controller did not perform as well in the experiments as in the numerical simulation. This is probably due to several factors. There was a significant dead zone in the motor due to friction, making it hard to operate the motor at slow speeds. The tilt sensor that was used on the platform had a sample rate of 20 samples per second, which was too slow to provide a smooth command signal to the amplifier. This resulted in jerky motor operation. Low resolution and noise in some sensors also hindered our ability to calculate the precise values of some quantities. The controller's experimental performance could be improved significantly by incorporating better sensors into the control system.

The numerical simulations predicted the experimental performance well, especially in the uncontrolled cases. A more complex mathematical model could be developed in order to predict the actual performance of the controller more accurately. This model could include the rigid body dynamics of the cargo, the elasticity of the cables, friction, air resistance, motor dynamics, and sensor dynamics. The model could also be formulated to sample quantities discretely as is done when the computer is executing the control algorithm.

We are currently investigating the use of the boom slew angle to control the out-of-plane pendulations. These two controllers working together will be a cost-effective solution to the problem of cargo transfer in rough seas since the only modification necessary to the crane would be the addition of a few sensors and electronic components. Other future work includes adding a routine in the control algorithm that will land the cargo safely on a lighter ship, which is moving relative to the craneship. The lighter ship will be simulated in the experimental setup by a second moving platform. This platform will have six degrees of freedom. The operator input will also be added to the control loop. After developing these concepts theoretically, we will test them on the scale model. In the future, we will perform experiments by feeding realistic ship-motion data to the ship-motion simulation platform.

Bibliography

[1] M. Abdel-Mooty and J. Roorda. Time delay compensation in active damping of structures. *Journal of Engineering Mechanics*, 117:2549–2570, 1991.

[2] J. Albus, R. Bostelman, and N. Dagalakis. The NIST RoboCrane. *Journal of Research of the National Institute of Standards and Technology*, 97(3), 1992.

[3] R. Bostelman and K. Goodwin. Survey of cargo handling research relative to the mobile offshore base (MOB) needs. Technical report, National Institute of Standards and Technology, Intelligent Systems Division, Gaithersburg, MD, July 1998. NIST Internal Report.

[4] S. L. Canfield. *Development of the Carpal Wrist: a Symmetric Parallel-Architecture Robotic Wrist*. PhD thesis, Virginia Polytechnic Institute and State University, May 1997.

[5] Joint Deployment Training Center. Additional JLOTS imagery. http://www.jdtc.eustis.army.mil/images/Addnl_JLOTS_images/additional_jlots_imagery.htm.

[6] U.S. Army Transportation Center. Sea state table. http://www.eustis.army.mil/weather/Weather_Products/seastate.htm.

[7] M. Clemens. Universal-joint coupling for connecting shafts. U. S. Patents, 125,880 & 125,881, 1872.

[8] Military Sealift Command. http://www.msc.navy.mil/inventory/.

[9] J. J. Craig. *Introduction to Robotics: Mechanisms and Control*. Addison Wesley Publishing Co., Reading, MA, 1989.

[10] T. I. Fossen. *Guidance and Control of Ocean Vehicles*. John Wiley & Sons, Chichester, UK, 1994.

[11] A. J. Ganino. Mechanical design of the carpal wrist: A parallel-actuated, singularity-free robotic wrist. Master's thesis, Virginia Polytechnic Institute and State University, May 1996.

[12] K. H. Hunt. *Kinematic Geometry of Mechanisms*. Oxford University Press, Oxford, Great Britian, 1978.

[13] A. H. Nayfeh. *Introduction to Perturbation Techniques*. John Wiley & Sons, Inc., New York, 1981.

[14] A. H. Nayfeh, C. Chin, and J. Pratt. Perturbation methods in nonlinear dynamics – applications to machining dynamics. *Journal of Manufacturing Science and Engineering*, 119:485–493, 1997.

[15] Joint Chiefs of Staff. Joint tactics, techniques, and procedures for joint logistics over-the-shore (JLOTS), November 1998. Joint Pub 4-01.6.

[16] N. Olgac and B. T. Holm-Hansen. A novel active vibration absorption technique: Delayed resonator. *Journal of Sound and Vibration*, 176(1):93–104, 1994.

[17] N. Olgac and W. Youping. On the stability of linear systems with unrelated time delays. In *ASME International Computers in Engineering Conference*, 1989.

[18] B. Padmanabhan, P. H. Tidwell, R. J. Salerno, and C. F. Reinholtz. VGT-based gimbals: Practical construction and general theory. In *Flexible Mechanisms, Dynamics, and Analysis, Proceeding of the 22nd Biennial Mechanisms Conference*, volume DE-Vol. 47, pages 437–443, 1992.

[19] C. L. Phillips and R. D. Harbor. *Feedback Control Systems*. Prentice-Hall, Inc., Englewood Cliffs, New Jersey, 1996.

[20] J. Rodeller, L. L. Chung, T. T. Soong, and A. M. Reinhorn. Experimental digital control of structures. *Journal of Engineering Mechanics*, 115:1245–1261, 1989.

[21] R. J. Salerno, S. L. Canfield, and C. F. Reinholtz. A parallel, four degree-of-freedom robotic wrist. In *Advances in Design Automation, Proceedings of the 1995 ASME Design Technical Conferences*, volume DE-Vol. 82, pages 765–771, 1995.

[22] T. G. Vaughters. Joint logistics over the shore operations. *Naval Engineers Journal*, 106(3):256–263, May 1994.

[23] W. J. Wang, C. C. Kao, and C. S. Chen. Stabilization, estimation, and robustness for large scale time-delay systems. *Control-Theory and Advanced Technology*, 7:569–585, 1991.

[24] B. Yang. Noncollocated control of a damped string using time delay. In *Proceedings of the 1991 American Control Conference*, volume 3, pages 2445–2448, 1991.

[25] K. Youcef-Toumi and O. Ito. A time delay controller for systems with unknown dynamics. *Transactions of the American Society of Mechanical Engineers, Journal of Dynamic Systems, Measurement, and Control*, 112:133–142, 1990.

Vita

Ryan James Henry was born on March 7, 1975 in Abington, Pennsylvania as the son of James and Virginia Henry. In 1984 he and his family moved to Maryland. After graduating from Severna Park High School, Ryan attended Virginia Tech and pursued a Bachelor's degree in Engineering Science and Mechanics. Deciding that he was not yet ready to leave Blacksburg, he declined offers from two other graduate schools and stayed at Virginia Tech to work towards a Master of Science degree in Engineering Mechanics. This summer he will move to Annapolis, Maryland and begin working for Northrop Grumman's Electronic Sensors and Systems Sector as a Mechanical Design and Development Engineer.